

# **X-ray Morphology of the Galaxy Group NGC 1550 with eROSITA**

Bruno da Rocha Schultz

Bachelorarbeit in Physik  
angefertigt im Argelander-Institut für Astronomie

vorgelegt der  
Mathematisch-Naturwissenschaftlichen Fakultät  
der  
Rheinischen Friedrich-Wilhelms-Universität  
Bonn

August 2024

DRAFT

Ich versichere, dass ich diese Arbeit selbstständig verfasst und keine anderen als die angegebenen Quellen und Hilfsmittel benutzt sowie die Zitate kenntlich gemacht habe.

Bonn, .....  
Datum .....  
Unterschrift

1. Gutachter: Prof. Dr. Thomas Reiprich
2. Gutachterin: Prof. Dr. Frank Bertoldi

---

## Acknowledgements

---

I would like to thank ...

You should probably use \chapter\* for acknowledgements at the beginning of a thesis and \chapter for the end.

DRAFT

*Context:* Galaxy groups like NGC 1550 play an important role in understanding the Universe's large-scale structure. They contain a significant fraction of the Universe's baryonic mass and are characterized by hot, ionized intragroup medium emitting X-rays, making X-ray observations essential for their study.

*Aims:* This thesis aims to characterize the X-ray morphology of the galaxy group NGC 1550 through surface brightness analysis in different directions, utilizing data from the *extended ROentgen Survey with an Imaging Telescope Array* (eROSITA).

*Methods:* Data from eRASS:1 was corrected and reduced for instrumental and background contamination. A  $\beta$ -model was fitted to the full azimuthal surface brightness profile, and sectoral analyses were conducted to compare the profiles across different regions of the galaxy group.

*Results:* NGC 1550 appears relaxed and spherically symmetrical. The  $\beta$ -model fit yielded a  $\beta$ -value of  $0.478 \pm 0.008$  and a core radius of  $r_c = (60 \pm 5)'' \approx (15 \pm 2)$  kpc. No significant deviations from spherical symmetry were found in the full azimuthal profile or in the sectoral analyses beyond  $390''$ . Discrepancies between observational and fitted background levels were noted, suggesting the need for improved background estimation.

---

# Contents

---

|          |  |           |
|----------|--|-----------|
| <b>1</b> | <b>Introduction</b>                                  | <b>1</b>  |
| <b>2</b> | <b>Theoretical Background</b>                        | <b>2</b>  |
| 2.1      | Clusters and Groups of Galaxies . . . . .            | 2         |
| 2.1.1    | The Intracluster Medium . . . . .                    | 2         |
| 2.1.2    | Emission Processes within the ICM . . . . .          | 2         |
| 2.1.3    | The $\beta$ -model of the ICM . . . . .              | 3         |
| 2.1.4    | The galaxy group NGC1550 . . . . .                   | 3         |
| 2.2      | eROSITA . . . . .                                    | 4         |
| 2.3      | Sky background and contamination sources . . . . .   | 4         |
| <b>3</b> | <b>Data Reduction</b>                                | <b>6</b>  |
| 3.1      | Raw photon images . . . . .                          | 6         |
| 3.2      | Image filtering . . . . .                            | 7         |
| 3.3      | Exposure map and image creation . . . . .            | 7         |
| 3.4      | PIB Correction . . . . .                             | 8         |
| 3.5      | Absorption Correction . . . . .                      | 8         |
| 3.6      | Exposure Correction . . . . .                        | 9         |
| 3.7      | Wavelet filtering and Point Source Removal . . . . . | 10        |
| <b>4</b> | <b>Data Analysis and Discussion</b>                  | <b>13</b> |
| 4.1      | Image Inspection and galaxy distribution . . . . .   | 13        |
| 4.2      | Full Azimuthal Surface Brightness Profile . . . . .  | 13        |
| 4.2.1    | $\beta$ -Model and Residual Image . . . . .          | 18        |
| 4.3      | Sectoral Surface Brightness Analysis . . . . .       | 19        |
| <b>5</b> | <b>Conclusion</b>                                    | <b>23</b> |
| 5.1      | Outlook . . . . .                                    | 24        |
| <b>A</b> | <b>Data Reduction</b>                                | <b>26</b> |
| A.1      | Exposure maps . . . . .                              | 26        |
| A.2      | PIB Map . . . . .                                    | 32        |
| A.3      | Orion-Eridanus Superbubble . . . . .                 | 33        |

|                        |           |
|------------------------|-----------|
| <b>Bibliography</b>    | <b>34</b> |
| <b>List of Figures</b> | <b>37</b> |
| <b>List of Tables</b>  | <b>38</b> |

DRAFT

# CHAPTER 1

---

## Introduction

---

Unlike the larger and more massive galaxy clusters, galaxy groups are smaller systems with typical masses around  $3 \times 10^{13} M_{\odot}$  (Schneider, 2006). Despite their relative modest size, the study of galaxy groups is fundamental to our understanding of the Universe's large-scale structure (LSS), as they likely contain a significant fraction of the total baryonic mass in the Universe (Fukugita, Hogan, and Peebles, 1998). The space between galaxy clusters and groups is characterized by a hot, ionized gas known as the intracluster medium (ICM) or the intragroup medium (IGM), which fills the space between the galaxies. This gas emits copious amounts of X-rays making X-ray observations an essential tool for identifying and studying these structures (Kravtsov and Borgani, 2012).

The galaxy group NGC1550, first linked to the extended X-ray source RX J0419+0225 through the ROSAT All-Sky Survey (Böhringer et al., 2000), has been the subject of extensive X-ray observations. Analysis have been conducted using data from various instruments, including ASCA (Kawaharada, Makishima, Takahashi, et al., 2003), XMM-Newton (Kawaharada, Makishima, Kitaguchi, et al., 2009), Chandra (Sun et al., 2003), and Suzaku (Sato et al., 2010). In this thesis, data gathered with the *extended ROentgen Survey with an Imaging Telescope Array* (eROSITA) shall be utilized to characterize the X-ray surface brightness profile of NGC1550 and compare the results with previous studies.

Following a brief overview of the theoretical background in Chapter 2, Chapter 3 will focus on reducing and correcting the data for instrumental and background contamination sources. Chapter 4 will analyze the surface brightness profile of NGC1550, including a beta model fitting of the full azimuthal profile. Additionally, the analysis will compare the north, south, east, and west sectors against each other and against the full azimuthal profile. Chapter 5 will summarize all results, offer suggestions for improvement and for future works.

# CHAPTER 2

---

## Theoretical Background

---

### 2.1 Clusters and Groups of Galaxies

Throughout the Universe, galaxies are not distributed homogeneously but are instead aggregated into large cosmic structures known as galaxy groups or galaxy clusters, which are the largest virialized structures in the Universe. Galaxy clusters typically have masses exceeding  $M \gtrsim 3 \times 10^{14} M_{\odot}$ , whereas galaxy groups have masses around  $M \sim 3 \times 10^{13} M_{\odot}$  (Schneider, 2006). Advancements in X-ray astronomy have demonstrated that these structures are significant sources of X-ray radiation (A. G. Cavaliere, Gurkaynak, and Tucker, 1971). This emission is well understood to originate from a hot intergalactic gas known as the intracluster medium (ICM)<sup>1</sup>, which is characterized by temperatures in the range of  $10^7$  to  $10^8$  K and constitutes the primary baryonic component of galaxy clusters and groups (Schneider, 2006).

#### 2.1.1 The Intracluster Medium

Within the deep gravitational wells of galaxy clusters and groups, the temperature becomes sufficiently high to fully ionize lighter elements and partially ionize heavier elements, resulting in the formation of a plasma. This hot, diffuse, and optically thin plasma, known as the intracluster medium (ICM), emits a significant amount of X-ray radiation. X-ray observations of the ICM have enabled a wide variety of cosmological studies including advances in understanding the large-scale structure formation in the Universe (Kravtsov and Borgani, 2012).

#### 2.1.2 Emission Processes within the ICM

A key principle of electrodynamics is that accelerated charges radiate energy. This radiation is referred to as bremsstrahlung or “free-free” when an unbound charged particle, typically an electron, is accelerated by the electric field of other charges, usually ions. In the ICM, this process predominates at temperatures above  $k_B T_e \gtrsim 2$  keV, where the total emissivity  $\epsilon_{\text{ff}}$  at solar metallicity scales

---

<sup>1</sup> The intercluster medium is also called the intragroup medium (IGM) in the case of galaxy groups. In the context of this thesis, the terms ICM and IGM will be used interchangeably, as a distinction between them is not necessary.

approximately as  $\epsilon_{\text{ff}} \propto T_e^{0.5} n_e^2$ , with  $n_e$  and  $T_e$  as the electron number density and temperature, respectively. At lower temperatures ( $k_B T \lesssim 2 \text{ keV}$ ), line emission becomes significant, with the emissivity being roughly described by  $\epsilon \propto T_e^{-0.6} n_e^2$ . Thus, for the low energy band 0.1 to 2.4 keV, one has a weak temperature dependence, i.e.  $\epsilon \propto n_e^2$ . (Reiprich and Pacaud, 2019).

### 2.1.3 The $\beta$ -model of the ICM

In the mid-1970s, (A. Cavaliere and Fusco-Femiano, 1976) laid the groundwork for the current understanding of the ICM. The X-ray morphology of clusters and groups is typically described by the beta model. This model assumes gas and galaxies share the same gravitational potential. Given a constant temperature  $T$  and velocity dispersion  $\sigma_r$ , the radial distributions of the gas  $n_{\text{gas}}$  and galaxies  $\rho_{\text{gal}}$  obey

$$\frac{n_{\text{gas}}(r)}{n_{\text{gas}}(0)} = \left[ \frac{\rho_{\text{gal}}(r)}{\rho_{\text{gal}(0)}} \right]^\beta ; \quad \beta = \frac{\mu m_p \sigma_r^2}{k_B T}$$

where  $\mu$  is the mean molecular mass,  $m_p$  is the proton mass and  $k_B$  is the Boltzmann constant. Using the King approximation  $\rho_{\text{gal}}(r) = \rho_{\text{gal}(0)} [1 + (r/r_c)^2]^{-3/2}$  (King, 1962), where  $r_c$  is the core radius and  $\epsilon \propto n_e^2$ , the X-ray surface brightness  $S_X$ , obtained by integrating over the emissivity, follows the profile

$$S_X(r) = S_X(0) \left[ 1 + \left( \frac{r}{r_c} \right)^2 \right]^{-3\beta+1/2}.$$

The beta model is widely used to describe cluster and group emissions, despite the assumptions listed above often being unmet. Excess core emission, for example, is typically addressed by adding a second beta model component:  $S_X^{\text{tot}} = S_{X,1} + S_{X,2}$  (Reiprich and Pacaud, 2019).

### 2.1.4 The galaxy group NGC1550

The galaxy group NGC1550 is located at a right ascension of  $64.9066^\circ$  and a declination of  $2.4151^\circ$ , with a redshift of  $z = 0.0123$  (Reiprich and Böhringer, 2002). Although the lenticular galaxy NGC 1550 has long been observable in the optical, it was first associated with the extended X-ray source RX J0419+0225 through the ROSAT All-Sky Survey (Böhringer et al., 2000). The presence of this extensive X-ray halo, along with its considerable mass ( $\sim 2 \times 10^{13} M_\odot$ ), led to its classification as a galaxy group (Kawaharada, Makishima, Takahashi, et al., 2003).

Recent studies indicate that NGC1550 does not meet the formal criteria for a fossil group (Sun et al., 2003; cf. Jones et al., 2003 for the criteria), but it shares several features with such groups. One notable characteristic is its high X-ray bolometric luminosity ( $\gtrsim 4.8 \times 10^{41} \text{ erg}$ ), which predominantly originates from a central, dominant, early-type galaxy. Fossil groups are thought to be formed when member galaxies in a regular galaxy group merge into a central dominant galaxy, and evidence for this process has been found in the metal distribution of NGC1550 (Kawaharada, Makishima, Kitaguchi,

et al., 2009; Sato et al., 2010). Additionally, a recent study has identified signs of AGN (active galactic nucleus) feedback and sloshing, suggesting a minor merger occurred around 33 million years ago (Kolokythas et al., 2020). While the group appears to be relaxed overall, a slight east-west elongation in the central region has been noted by multiple authors (Kolokythas et al., 2020; Sun et al., 2003).

## 2.2 eROSITA

The *extended ROentgen Survey with an Imaging Telescope Array* (eROSITA) is a highly sensitive, wide-field X-ray telescope designed to capture deep images across large areas of the sky. Mounted on the Spektrum-Roentgen-Gamma (SRG) observatory in a halo orbit around the second Lagrange Point (L2), eROSITA operates within the 0.2 to 10.0 keV energy range. It is the first instrument to perform an all-sky imaging survey in the hard X-ray band (2.0 to 10.0 keV). In the soft X-ray band (0.5 to 2.0 keV), eROSITA boasts a sensitivity greater than that of its predecessor, the ROSAT All-Sky Survey. eROSITA features seven identical mirror modules, known as Telescope Modules (TMs), with 54 mirror shells in Wolter-I geometry and a 1.6-meter focal length. Five TMs (TM1, TM2, TM3, TM4 and TM6) have aluminum on-chip optical light filters and are collectively referred to as TM8. The remaining two TMs (TM5, TM7), designed for low-energy spectroscopy, lack these filters and are referred to as TM9. Collectively, TM8 and TM9 are referred to as TM0. (Predehl, P. et al., 2021). In this thesis, data from the first all-sky survey (eRASS:1) will be utilized. The data is provided in the form of event lists, which essentially detail the spatial position of X-ray photon arrivals on the detector, their time of arrival, and their energy. The event lists are made available in  $3.6^\circ \times 3.6^\circ$  regions known as skytiles.

## 2.3 Sky background and contamination sources

For a thorough analysis of X-ray photons, it is essential to carefully consider both external background and internal instrumental contamination effects. The following section will provide a brief overview of the most important factors relevant to this analysis.

**Cosmic X-ray Background (CXB):** The cosmic X-ray background (CXB) comprises multiple sources, including diffuse, unabsorbed thermal emissions from the Local Hot Bubble, a plasma cavity surrounding the Sun, and absorbed thermal emissions from the Galactic halo (Galeazzi et al., 2007). Additionally, it includes discrete extragalactic sources, predominantly unresolved AGNs (Brandt and Hasinger, 2005). The diffuse component is more prominent in the lower energy band  $\sim 1$  keV, while the extragalactic sources dominate at higher energies. In this analysis, background emission from the nearby Orion-Eridanus superbubble, which spans roughly  $40^\circ$  on the sky, shall also be present, as it emits in the soft X-ray regime (Krause et al., 2014). Figure 2.1, taken from (Krause et al., 2014), shows an X-ray map of the Orion-Eridanus superbubble in the 0.5 to 2.0 keV band, illustrating its overlap with the emission from the galaxy group NGC1550.

**Non-X-ray Background (NXB):** The non-X-ray background consists of two main components: highly variable soft protons flares (SPF) from the solar corona and Earth's magnetosphere, which

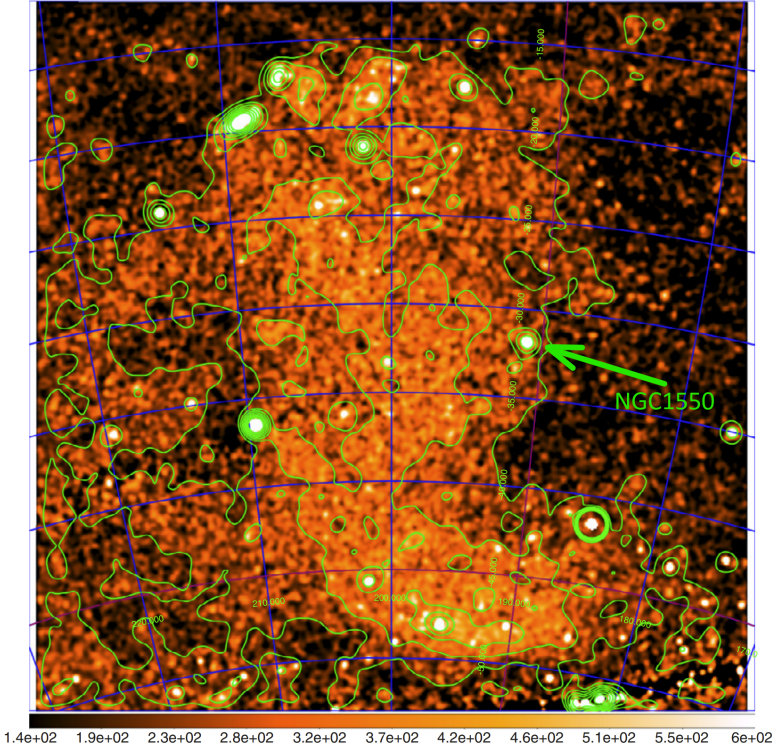


Figure 2.1: X-ray map in galactic coordinates of the Orion-Eridanus superbubble in the 0.5 to 2.0 keV band from the ROSAT all-sky survey. The colorbar units are  $10^{-6} \text{ cts} \cdot \text{arcmin}^{-2} \text{s}^{-1}$  and the contour levels are 220, 300, 380, 460, 540, 620, 700. The image was taken from (Krause et al., 2014). The green arrow and label were added to highlight the position of NGC1550.

can be focused onto detectors, and energetic Galactic Cosmic Ray (GCR) primaries, which interact with the detector to produce secondary particles. The secondary particles can deposit charge in the detector, making it challenging to distinguish them from true X-ray events. This is generally referred to as the particle-induced background (PIB) (Bulbul et al., 2020).

**eROSITA light leak:** Shortly after the launch of eROSITA, it was observed that CCDs lacking an on-chip filter (TM9) recorded a notably higher number of events. This was attributed to optical and ultraviolet light from the Sun entering the CCD through an unidentified gap in the detector shielding, and was subsequently termed “light-leak” (Predehl, P. et al., 2021).

**$N_{\text{H}}$  absorption:** As X-rays travel to the detector, they undergo photoelectric absorption in the interstellar and intergalactic medium. The cross-section  $\sigma \propto E^{-3}$  is inversely proportional to energy, causing a bias toward harder X-rays, as they interact less. Additionally, the cross-section is proportional to the atomic number,  $\sigma \propto Z^5$ , making metal abundance crucial for energies  $\gtrsim 0.2 \text{ keV}$  (Willingale et al., 2013).

# CHAPTER 3

---

## Data Reduction

---

In the following section, the underlying data shall be reduced and corrected for the various effects and sources of contamination explained in Section 2.3. Data from eRASS:<sup>1</sup> and all TMs (1-7) is used, which were processed with the eROSITA pipeline processing version c010. The galaxy group NGC1550 is located in skytile 065087. Additionally, the surrounding skytiles 062084, 062087, 062090, 065084, 065090, 068084, 068087, and 068090 are used to cover regions up to  $\sim 3R_{200}$  (cf. value below). Data reduction is performed with the software HEASoft version<sup>2</sup> 6.29 and the extended Science Analysis Software System<sup>3</sup> (eSASS 4DR1).

Values for  $R_{200}$  and  $R_{500}$  were taken from Reiprich and Böhringer, 2002 and converted to  $R_{200} = 58.58'$  and  $R_{500} = 37.15'$  based on the cosmology used in this paper. The cosmology assumes  $\Omega_m = 0.3$ ,  $\Omega_\Lambda = 0.7$  and  $h = 0.7$ , with  $1'' = 0.252$  kpc at the redshift  $z = 0.0123$  of the galaxy group.

### 3.1 Raw photon images

Prior to the data reduction process, raw photon images for all combined skytiles and TMs are presented across the following energy bands: 0.2 to 2.3 keV, 2.3 to 6.0 keV, and 6.0 to 9.0 keV. The skytiles were combined using the *eSASS* task `evtool` with no additional parameters applied to show all inherent deficiencies. The raw photon images are presented in Figure 3.1. It is evident that the counts are noticeably lower in the right half of each image. This issue will be addressed in detail through the absorption and exposure correction in Section 3.6. As can be observed, the group emission is mainly concentrated in the lower energy band, making the low energy band the focus for detecting emission structures. In this analysis, the 0.2 to 2.3 keV energy band is used. However, due to the light-leak in TM9 the energy range is restricted to 0.8 to 2.3 keV, while it remains 0.2 to 2.3 keV for TM8. Henceforth, this TM-dependent energy band will be referred to as the “soft-band” and the 6.7 to 9.0 keV energy range will be designated the “hard-band”.

<sup>1</sup> [https://erosita.mpe.mpg.de/dr1/AllSkySurveyData\\_dr1/](https://erosita.mpe.mpg.de/dr1/AllSkySurveyData_dr1/) (Last accessed: 05.08.2024)

<sup>2</sup> <https://heasarc.gsfc.nasa.gov/docs/software/heasoft/> (Last accessed: 04.08.2024)

<sup>3</sup> <https://erosita.mpe.mpg.de/dr1/eSASS4DR1/> (Last accessed: 04.08.2024)

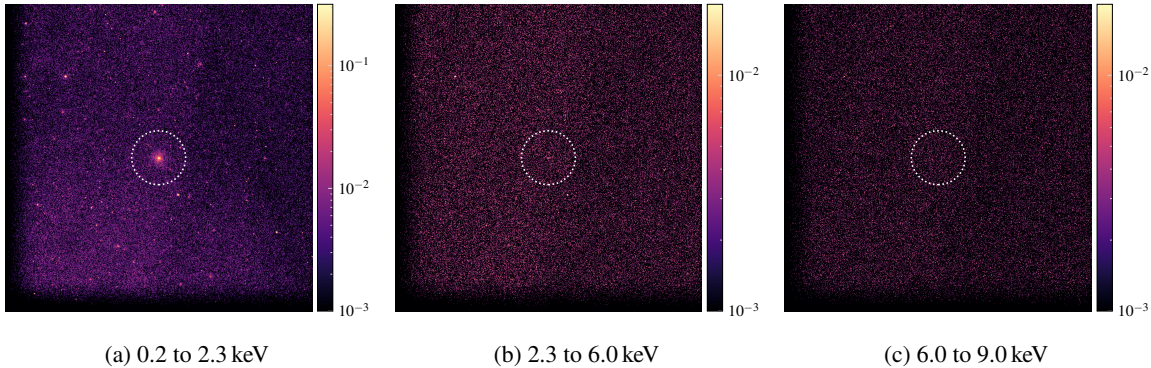


Figure 3.1: Raw photon images from TM0 of all combined skytiles centered around NGC1550, displayed in the energy bands 0.2 to 2.3 keV (a), 2.3 to 6.0 keV (b), and 6.0 to 9.0 keV (c), with Gaussian smoothing of 4 pixels. The colorbar represents (smoothed) photon counts. For visualization purposes, different cuts were used for the middle and right image and  $R_{200}$  is shown (white dashed circle). The majority of the group emission is visible in the lower energy band (0.2 to 2.3 keV).

## 3.2 Image filtering

Each skytile is cleaned individually using `evtool` with `pattern=15` to select all event patterns (single, double, triple and quadruple) and `flag=0xe00fff30` to remove bad pixels and CCD corners. Subsequently, soft proton flares are identified and mitigated through the following process: the `flaregti` task is employed to generate light curves with 20 s time bins in the energy range of 5 to 10 keV. A  $3\sigma$  threshold is then determined; time intervals where count rates exceed this threshold are likely due to soft proton flares. Subsequently, the task `flaregti` is then rerun using the aforementioned threshold to establish good-time-intervals (GTIs) excluding these flare periods, which are applied using `evtool` with the `gti="FLAREGTI"` parameter. All SPF-filtered and cleaned skytiles are combined into a single TM0 photon image using `evtool`. From this point onwards, these combined images shall be referred to as “filtered”.

## 3.3 Exposure map and image creation

The `evtool` task, in conjunction with the `telid` parameter, is used to split the TM0 filtered photon images into individual filtered images for each TM. These images are then resized to the soft-band and the hard-band using `evtool` with the parameters `emin` and `emax`. Both vignetted and flat (non-vignetted) exposure maps are generated for each TM in the soft-band using the `expmap` task with the `withvignetting` parameter. These maps are utilized for subsequent PIB and exposure corrections. Moreover, the `withdetmaps` parameter is specified to crop the images at the edge of the field of view for each TM. By keeping `withmergedmaps` at its default value of YES, merged all-telescope exposure maps are created. This means the exposure maps consider the 7 TMs as one TM with on-chip TM, assuming the combined effective area of the 7 on-chip TMs. The vignetted and flat exposure maps are available in Appendix A.1.

### 3.4 PIB Correction

It is necessary to subtract the particle-induced background (PIB) from the combined filtered photon image. The following approach is based on extensive studies of the eROSITA filter wheel closed (FWC) data conducted by Dr. F. Pacaud, as utilized for example in Reiprich, Veronica, et al. (2021). The PIB is modeled for each TM using FWC data. Given the minimal spatial variation of the PIB, this modelling employs the flat exposure map created in Section 3.3. Furthermore, due to the negligible spectral variation, the counts  $H_{\text{obs}}$  in the hard band, where PIB counts dominate, are used to estimate the PIB contribution in the soft-band by multiplication with the ratio  $R$  of the number of FWC counts in the soft band  $S_{\text{FWC}}$  to the hard band  $H_{\text{FWC}}$ . The PIB-map for each TM is then generated by applying this factor to the flat exposure map, normalized to 1 by dividing by the sum of all pixel values (norm. flat exposure map). Therefore, the PIB map of a given TM is given by

$$\text{PIB map}_{\text{TM}} = H_{\text{obs}} R \cdot (\text{norm. flat exposure map}).$$

Soft-band, PIB-corrected image are obtained by subtracting the PIB map of each TM from the respective soft-band, filtered photon image. The complete image for TM0 is obtained by co-adding all PIB-corrected images. To better visualize the PIB-correction, individual background maps are also co-added to form a complete PIB map, which can be found in Appendix A.2. Additionally, Appendix A.1 contains the obtained  $H_{\text{obs}}$  and  $R$  values.

### 3.5 Absorption Correction

As previously outlined in Section 2.3, X-ray absorption by the ISM must be taken into account. To correct for this absorption, the methodology outlined in Reiprich, Veronica, et al. (2021) is followed. Furthermore, scripts for the absorption correction were provided by Angie Veronica (as utilized in Veronica, 2020). At energies  $\gtrsim 0.2$  keV, as is relevant for this analysis, the absorption of X-rays by metals play a significant role (cf. 2.3). Assuming solar metallicity, the hydrogen column density ( $N_{\text{H}}$ ) can be used to trace the absorbing material. A cutout of the HI4PI all-sky survey (HI4PI Collaboration et al., 2016) is reprojected onto the field of view of the combined tile image to create a neutral atomic hydrogen map ( $N_{\text{HI}}$ -map). Additionally, as outlined in Willingale et al. (2013), a molecular hydrogen map ( $N_{\text{H}_2}$ -map) is constructed by dividing the full sky image into  $52 \times 52$  pixel cells, querying  $N_{\text{H}_2}$  values from the Swift homepage<sup>4</sup>, and distributing these values across each cell. The total hydrogen column density map, constructed by  $N_{\text{Htot}} = N_{\text{H}} + 2N_{\text{H}_2}$ , is shown in Figure 3.2, with  $N_{\text{H}}$  ranging from  $N_{\text{Htot}, \text{min}} = 2.91 \times 10^{20} \text{ cm}^{-2}$  to  $N_{\text{Htot}, \text{max}} = 1.61 \times 10^{21} \text{ cm}^{-2}$ .

Subsequently, for each individual value of  $N_{\text{H}}$  in the  $N_{\text{Htot}}$ -map, the expected soft band count rates for TM1 and TM5 – which serve as proxies for TM8 and TM9, respectively – are simulated for the model

$$\text{apc}_{\text{LHB}} + \text{tb}_{\text{abs.}} \cdot (\text{apc}_{\text{MWH}} + \text{pow})$$

---

<sup>4</sup> <https://www.swift.ac.uk/analysis/nhtot/index.php> (Last accessed: 25.07.2024)

using the X-ray spectral fitting package XSPEC<sup>5</sup> (Arnaud, 1996) with the `fakeit` command and their respective area (ARF) and response files (RMF). Here,  $\text{apc}_{\text{LHB}}$  represents unabsorbed Local Hot Bubble emission,  $\text{tb}_{\text{abs}}$  the absorption along the line of sight,  $\text{apc}_{\text{MWH}}$  the absorbed Milky Way Halo emission, and  $\text{pow}$  the absorbed emission from unresolved point sources (e.g., AGNs). A correction factor  $A_{\text{corr}}$  is determined for each value of  $N_{\text{H}}$  by dividing the simulated count rate for the  $N_{\text{Htot}}$ -map median ( $\overline{N_{\text{Htot}}}$ ) by the simulated count rate of the  $N_{\text{H}}$  of interest, hence

$$A_{\text{corr}}(N_{\text{H}}) = \frac{\text{simulated count rate}(\overline{N_{\text{Htot}}})}{\text{simulated count rate}(N_{\text{H}})}.$$

Finally, each  $N_{\text{H}}$  in the  $N_{\text{Htot}}$ -map is replaced by the corresponding correction factor  $A_{\text{corr}}$  to create an absorption correction map. Absorption correction maps are created for both TM1 and TM5.

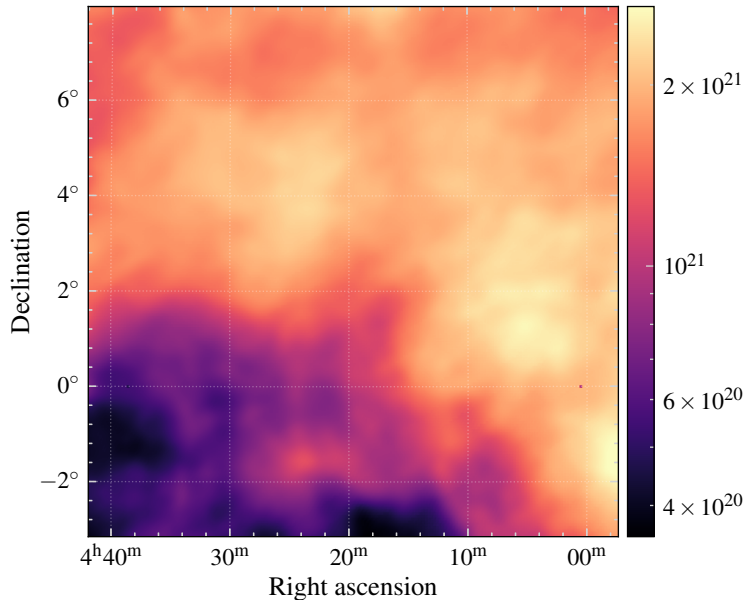


Figure 3.2:  $N_{\text{Htot}}$ -map obtained by reprojecting the HI4PI all-sky survey and querying  $N_{\text{H}_2}$  values from the Swift homepage. The color bar units are  $\text{cm}^{-2}$ .

### 3.6 Exposure Correction

The count image of any given X-ray observation is inherently dependent on a detector's effective area and the telescope's pointing motion throughout the observation. In order to obtain meaningful flux units (e.g.  $\text{cts} \cdot \text{arcsecond}^{-2} \text{s}^{-1}$ ), these effects must be considered. This is accomplished by dividing the count image by the vignetted exposure map created in Section 3.3, thereby rescaling all segments of the count image to the same relative exposure (Davis, 2001). However, an exposure map must be

<sup>5</sup> <https://heasarc.gsfc.nasa.gov/xanadu/xspec/> (Last accessed: 25.07.2024)

created separately for TM8 and TM9 for three reasons: first, TM9 uses a narrower energy band, which lowers its expected count rate; second, this narrower energy band necessitates a different absorption correction map; third, TM8 and TM9 have very distinct area response files because of their different filter configurations. Therefore, it is not possible to simply combine the two exposure maps as they must first be corrected for these effects. The procedure outlined in Reiprich, Veronica, et al. (2021) will be followed.

First, the vignetted exposure map of TM8 and TM9 are divided by their respective absorption correction maps to obtain an absorption-corrected exposure map ( $\text{exmap}_{\text{TM8, corr}}$ ,  $\text{exmap}_{\text{TM9, corr}}$ ). Second, the ratio of PIB-corrected count rates of TM8 and TM9 is used to define a correction factor

$$E_{\text{corr}} = \frac{\text{PIB corr. count rate(TM9)}}{\text{PIB corr. count rate(TM8)}}.$$

The total absorption-corrected exposure map for TM0 is then given by

$$\text{exmap}_{\text{TM0, corr}} = \text{exmap}_{\text{TM8, corr}} + E_{\text{corr}} \cdot \text{exmap}_{\text{TM9, corr}}$$

A correction factor of  $E_{\text{corr}} = 0.4628$  is obtained and the resulting absorption-corrected TM0 exposure map can be found in Appendix A.1. The final filtered, PIB-corrected, absorption-corrected, and exposure-corrected soft-band image is obtained by dividing the filtered and PIB-corrected soft-band TM0 image by its absorption-corrected exposure map. Henceforth, this will be referred to as the “corrected” soft-band image. An examination of the exposure map shows that the lower counts observed on the right side of each image in Figure 3.1 were due to a count enhancement in the left portion of each image. However, this issue has now been rectified through the absorption and exposure correction.

Figure 3.3 compares the filtered, full energy-band count rate image (the filtered full band count image divided by its respective exposure map) with the corrected soft-band image, both smoothed using a Gaussian kernel of 12 pixels. It is evident that group emission can be much better distinguished from the background in the corrected soft-band image.

### 3.7 Wavelet filtering and Point Source Removal

It is necessary to remove the emission from point-like sources (e.g. AGNs) and unrelated extended sources to avoid interfering with the group emission under study. This is achieved using the wavelet filtering pipeline as described in Pacaud et al. (2006). The wavelet transform decomposes an image  $I(x, y)$  into coefficients  $(w_1, \dots, w_n, c_n)$

$$I(x, y) = c_n(x, y) + \sum_{j=1}^n w_j(x, y).$$

Here,  $c_n(x, y)$  is the smoothed image, and  $w_j(x, y)$  essentially represents the contribution of a wavelet function at a scale  $j$  and position  $(x, y)$  to the total image. By retaining only the coefficients that

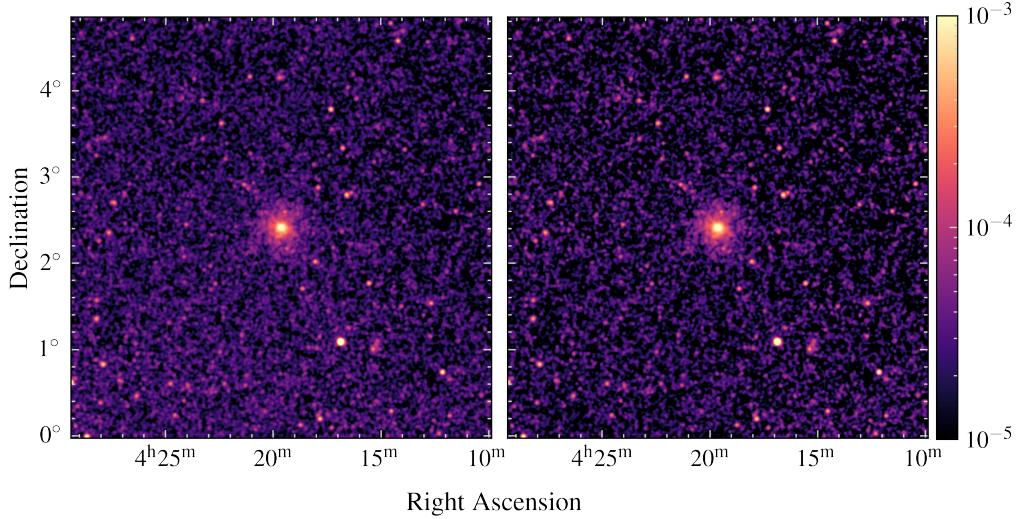


Figure 3.3: Comparison between the filtered, full energy-band count rate image (left) and the final corrected, soft-band count rate image (right), both smoothed using a Gaussian kernel of 12 pixels. The corrected image clearly shows improved differentiation of group emission from the background in comparison to the filtered, full band image.

satisfy

$$|w_j(x, y)| > k\sigma_j,$$

where  $\sigma_j$  is the standard deviation at scale  $j$  and  $k$  is a clipping factor, and then applying the inverse wavelet transform, an image is obtained that includes only significant scales, i.e. those that are not due to noise (Starck, J.-L. and Pierre, M., 1998). The resulting image is called a wavelet-filtered image.

In the pipeline being used, the absorption-corrected exposure map,  $\text{exmap}_{\text{TM0, corr}}$ , and the filtered photon image are used to account for the previous data reduction and to statistically treat the Poisson noise. After wavelet filtering, a source catalog is obtained by SExtractor (Bertin and Arnouts, 1996). This is made possible by the significant noise reduction and smoothed background achieved by the wavelet filtering. The extended X-ray emission near NGC1550 is manually removed from the catalog, and a cheese mask is created from the catalog and applied to  $\text{exmap}_{\text{TM0, corr}}$ . Emission around unrelated, but projectionally close, clusters and groups is also manually added to the cheese mask. Repeating the wavelet filtering with the cheese-masked map reduces ringing artifacts that typically occur near bright sources with steep flux gradients, and allows the detection of the previously missed sources. Figure 3.4 compares the wavelet filtering before and after applying of the cheese mask to the exposure map. Furthermore, the complete data reduction workflow described in this chapter is briefly summarized in Figure 3.5

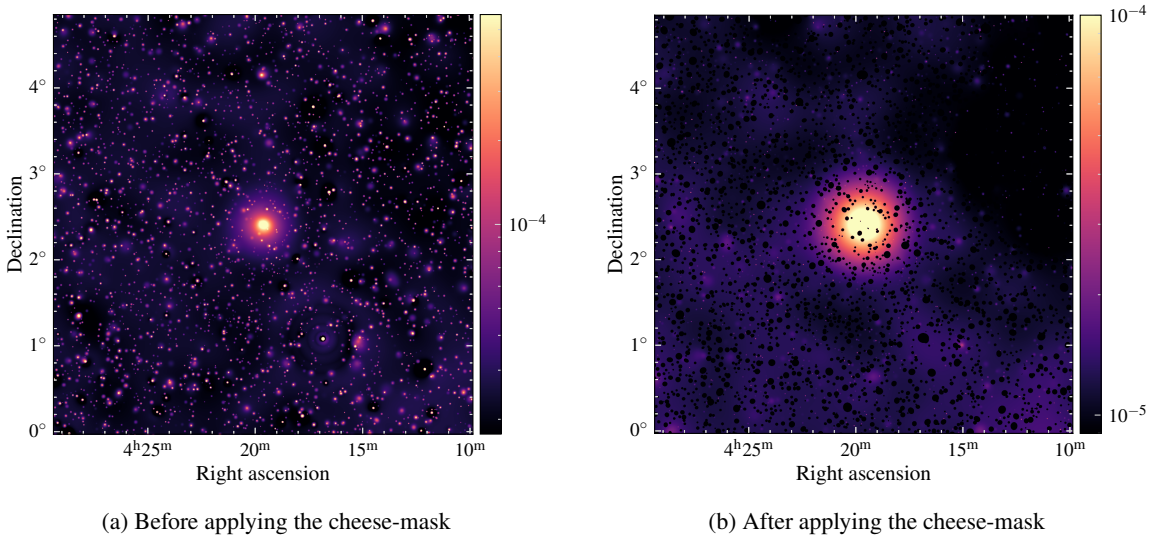


Figure 3.4: Corrected wavelet filtered image before (a) and after (b) applying the cheesemask. The left image is normalized such that the ringing artifacts are more prominent. The cheese-masked image has significantly reduced ringing artifact and group emission is well visible.

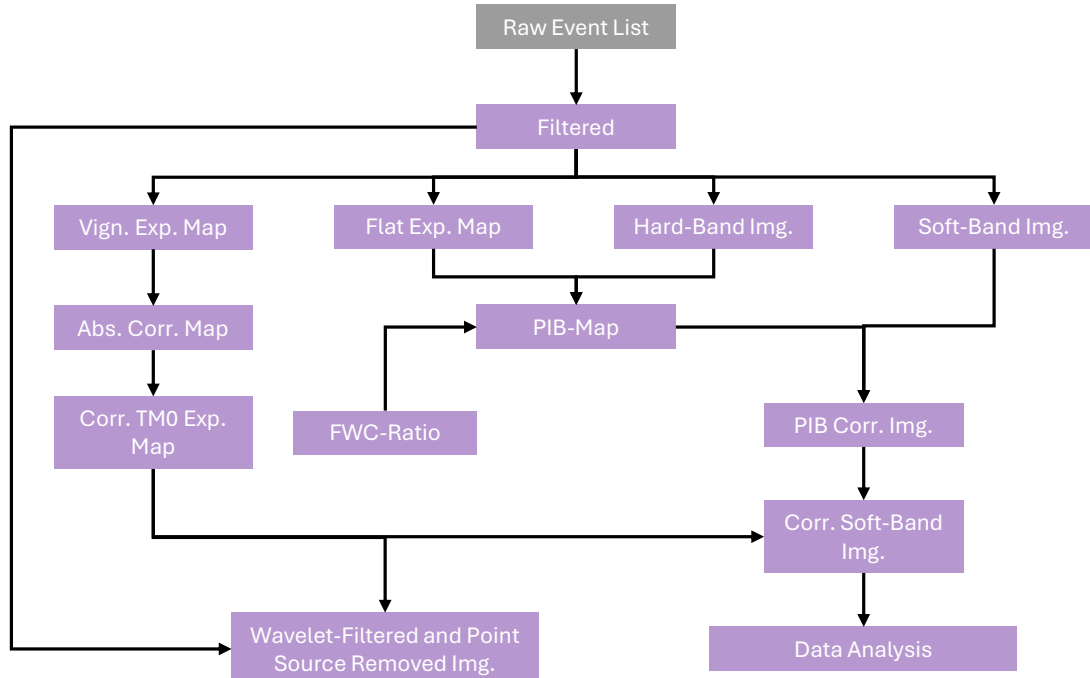


Figure 3.5: Workflow diagram summarizing the data reduction procedures described in this chapter.

# CHAPTER 4

---

## Data Analysis and Discussion

---

### 4.1 Image Inspection and galaxy distribution

A contour plot of the corrected and cheese-masked wavelet-filtered image is shown in Figure 4.1 to visualize emission beyond  $R_{500}$  more clearly. Furthermore, the galaxy distribution using data from NASA/IPAC Extragalactic Database (NED) is extracted within a  $1^\circ$  radius of the galaxy group NGC 1550 and overlayed. There are 26 galaxies with similar redshifts  $0.010 \leq z \leq 0.015$  including the galaxy NGC1550 ( $z = 0.0123$ ) itself. From Figure 4.1 it is clear that the group appears spherically symmetrical and relaxed. Beyond  $R_{500}$ , emission becomes difficult to distinguish from the background, which is fairly complex due to the Orion-Eridanus superbubble (cf. Appendix A.3 for a closer inspection). There is a noticeable gradient in the background emission, with a lower background to the north compared to the south. The galaxy distribution is loosely clustered to the northeast, but no clear correlation with the X-ray contours is observed. Usually, this helps indicate whether excess emission along a certain direction is significant.

To highlight emission structures within  $R_{500}$ , Figure 4.2 presents a contour plot of the corrected soft-band image smoothed with a Gaussian kernel of 8 pixels. Within this radius, some deviations from perfect azimuthal symmetry are noticeable. A slight east-west elongation within approximately  $390''$  (inner circle in the figure) can indeed be inferred as mentioned in Section 2.1.4. Beyond  $390''$ , features are harder to distinguish: the emission in the north, south and east appear slightly more irregular. Emission in the west, falls more uniformly and there seems to be slight emission dip between  $390''$  and  $810''$  (outer circle in the figure) compared to the other sectors.

### 4.2 Full Azimuthal Surface Brightness Profile

To more accurately identify or exclude potential deviations from spherical symmetry, surface brightness (SB) analysis will be performed. First, the emission center is estimated by constructing a  $2'$  aperture around the apparent center (right ascension  $64.9066^\circ$  and a declination  $2.4151^\circ$ ). This aperture size is chosen to capture a statistically significant number of photons without leaving the group center. The flux-weighted average coordinates of the fully corrected image within this aperture

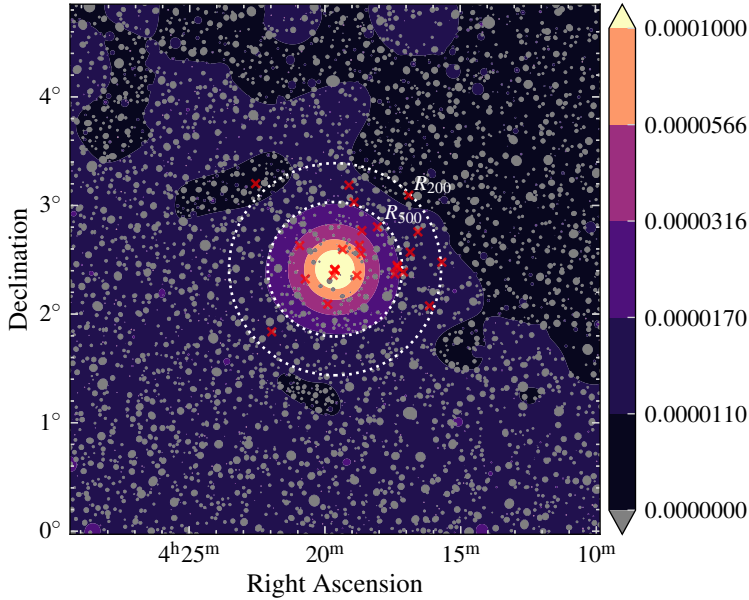


Figure 4.1: Contour plot of the corrected, cheese-masked, wavelet-filtered image with overlaid galaxy distribution (red crosses) within a  $1^\circ$  radius of NGC 1550. The color bar represents counts per second. The plot shows a distinct emission boundary at  $R_{500}$ , with emission beyond this radius becoming difficult to distinguish from the background. The galaxy distribution is clustered to the northeast, though no clear correlation with the X-ray contours is observed.

yields a right ascension of  $64.909^\circ$  and a declination of  $2.414^\circ$  and shall be referred to as the SB-center. Concentric annulli of  $1'$  width are constructed from the SB-center up to an angular distance of  $80' \approx 1.5R_{200}$ . The counts  $C$  within each annulus are determined using the `funcnts` task from the `funtools` software, with a Poisson error of  $\sqrt{C}$ . The surface brightness  $S$  for each annulus is calculated by

$$S = \frac{C_{\text{filt}} - C_{\text{PIB}}}{C_{\text{expmap}} \cdot A},$$

where  $C$  denotes the counts in the filtered photon image, total PIB map, and exposure map, respectively, and  $A$  is the annulus area. Errors are calculated using Gaussian error propagation. Furthermore, background estimation is performed using 10 circular regions with a  $30'$  radius, each centered at a distance of  $100'$  from the SB-center (Figure 4.3). The average background surface brightness is evaluated for all circles combined and separately for the northern (circles 1-5) and southern region (circles 6-10) to account for the background gradient. Table 4.1 lists the average background for all 3 cases. As is clear from the table, the total background level is consistent with the other two within  $1\sigma$ . Therefore, unless otherwise specified, the total background value derived from all circles will be used for the subsequent analysis and interpretation. A  $\beta$ -model (cf. Section 2.1.3) is employed to

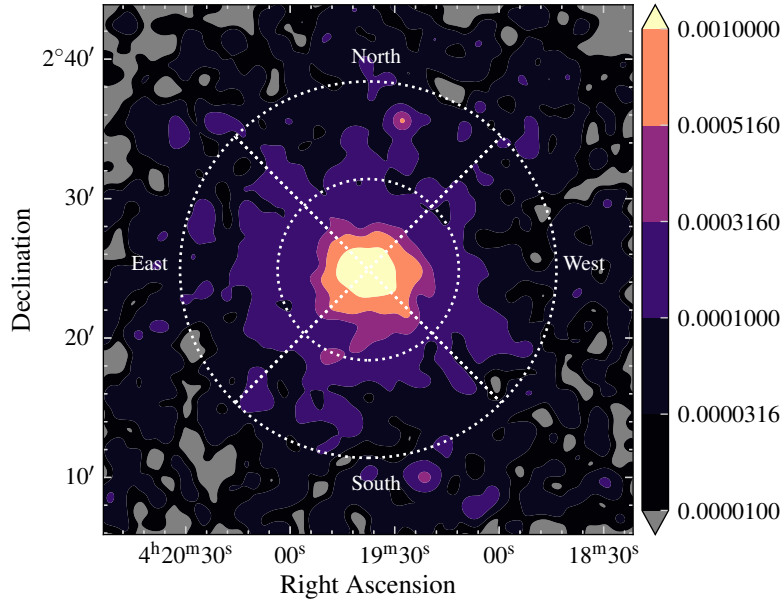


Figure 4.2: Contour plot of the corrected soft-band image smoothed with a Gaussian kernel of 8 pixels. The color bar indicates counts per second. Some deviations from azimuthal symmetry are observed within the outer circle ( $\sim 810''$ ). The inner circle denotes a radius of  $\sim 390''$ . Within this region, an east-west elongation of the core is noticeable. The four wedges labeled north, south, east, and west correspond to the angular (but not radial) ranges used to extract surface brightness.

| Region | Background / $\text{cts s}^{-1} \text{arcsec}^{-2}$ |
|--------|---|
| North  | $(1.03 \pm 0.10) \times 10^{-7}$                    |
| South  | $(1.27 \pm 0.04) \times 10^{-7}$                    |
| Total  | $(1.15 \pm 0.14) \times 10^{-7}$                    |

Table 4.1: Surface brightness and associated errors for the different background regions: north (circles 1-5), south (circles 6-10) and total (all circles).

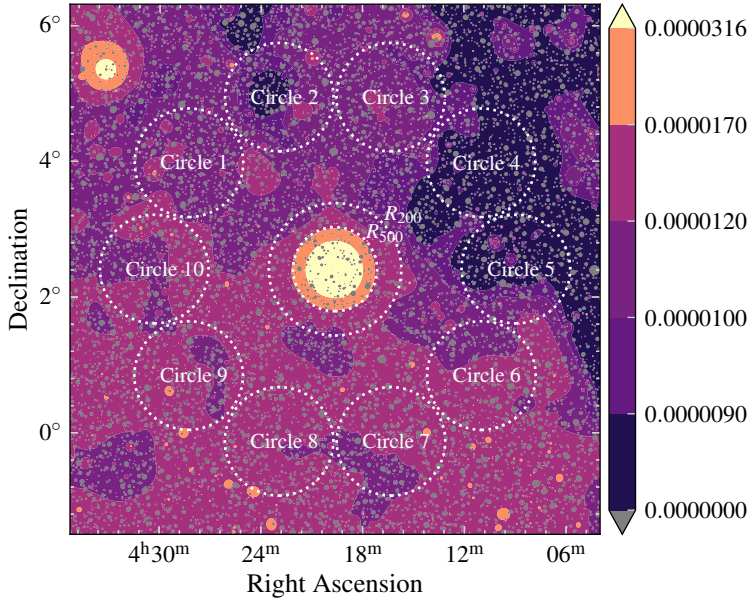


Figure 4.3: Background estimation. Depicted are 10 circular regions utilized to estimate the observed background. Circles 1-5 correspond to the northern background, and circles 6-10 to the southern background. The total background corresponds to all circular regions. The obtained values can be found in Table 4.1.

characterize the surface brightness profile, given by

$$S_X(r) = S_X(0) \left( 1 + \left( \frac{r}{r_c} \right)^2 \right)^{-3\beta+0.5} + d$$

where  $d$  represents the background emission. The center of each annulus is taken to be  $r$  and the corresponding surface brightness values are utilized. The optimized parameters and  $\chi^2/\text{d.o.f}$  (chi squared per degrees of freedom) are listed in Table 4.2. Figure 4.4 illustrates the surface brightness as a function of radial distance from the center, including both the fitted  $\beta$ -model and the observationally estimated background level.

| Parameter               | $S_0 / \text{cts s}^{-1} \text{arcsec}^{-2}$ | $\beta$           | $r_c / ''$ | $d / \text{cts s}^{-1} \text{arcsec}^{-2}$ |
|-------------------------|--|-------------------|------------|--|
|                         | $(4.1 \pm 0.4) \times 10^{-5}$               | $0.478 \pm 0.008$ | $60 \pm 5$ | $(9.3 \pm 0.4) \times 10^{-8}$             |
| $\chi^2/\text{d. o. f}$ | 0.96   |                   |            |  |

Table 4.2: Fit parameters, their errors, and the reduced chi-squared value for the full azimuthal surface brightness profile.

The  $\beta$ -model fit for the surface brightness profile, shown in Figure 4.4, yields  $\beta = 0.478 \pm 0.008$  and a core radius  $r_c = (60 \pm 5)'' \approx (15 \pm 2) \text{kpc}$  with  $\chi^2/\text{d.o.f.} = 0.96$ . This result is consistent

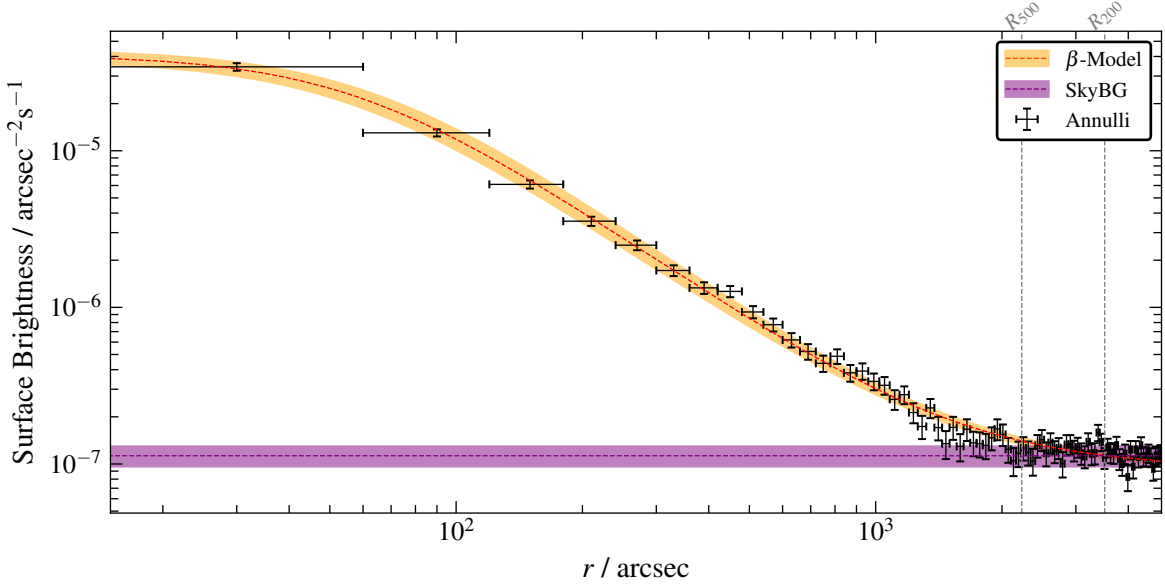


Figure 4.4: Surface brightness within each annulus (black crosses) as a function of distance from the determined SB-center including error bars. The dashed orange line represents the best  $\beta$ -model fit, while the purple line indicates the observationally determined background. The shaded regions correspond to their respective  $1\sigma$  intervals.

with previous studies: (Kawaharada, Makishima, Takahashi, et al., 2003) report  $\beta = 0.47$  and  $r_c \approx (16 \pm 1)$  kpc using ASCA data; (Kawaharada, Makishima, Kitaguchi, et al., 2009) use a double  $\beta$ -model to find  $\beta = 0.50 \pm 0.05$  and  $r_c \approx (20 \pm 3)$  kpc for the outer component from XMM-Newton data; (Sun et al., 2003) also derive  $\beta \sim 0.48$  and a slightly higher  $r_c \approx 26$  kpc for the outer component using Chandra data; (Reiprich and Böhringer, 2002), although, report a somewhat higher  $\beta = 0.554^{+0.049}_{-0.037}$  using ROSAT. The surface brightness profile also highlights that the group emission decreases to the background level at approximately  $R_{500}$ , as observed in Section 4.1. The observationally estimated total background in Table 4.1, however, is approximately 24% higher than the background obtained by the  $\beta$ -model fit (cf. Table 4.2) at  $1.5\sigma$ . Although this discrepancy is not too alarming, it does indicate challenges associated with the complex background, implying that they could have been chosen more carefully.

A double  $\beta$ -model fit was not successful. This can be attributed to the angular resolution of the 1' width annulli, limiting the ability to resolve the inner core emission. Performing a  $\beta$ -model fit with finer annuli was attempted, but this did not significantly improve the description of the surface brightness profile within the core and resulted in poor error estimation in the outskirts due to low count rates. Indeed, (Kawaharada, Makishima, Kitaguchi, et al., 2009) find an inner core component of  $r \sim 3$  kpc corresponding to  $\approx 12''$  which is comparable to the eROSITA angular resolution  $\sim 15''$  (Predehl, P. et al., 2021). A successful two- $\beta$  model, however, might be possible by fixing the inner core radii or convolving the model with the eROSITA point spread function, but this was not attempted within the scope of this thesis.

### 4.2.1 $\beta$ -Model and Residual Image

Using the parameters from Table 4.2, a  $\beta$ -model image (Fig. 4.5) and a residual image (Fig. 4.6) are created. The  $\beta$ -model image is generated by distributing the one-dimensional  $\beta$ -model across the image. This involves computing the distance from the surface brightness center to each coordinate  $(x, y)$  in the image and then scaling the output of the  $\beta$ -model by the eROSITA pixel area of  $16\text{arcsec}^2$ . The residual image (res. img) was obtained by subtracting the scaled  $\beta$ -model from the corrected soft-band image (corr. img). Hence,

$$\text{res. img}(x, y) = \text{corr. img}(x, y) - S \left( \sqrt{x^2 + y^2} \right) \cdot \text{pix. area.}$$

The residual image indicates that the  $\beta$ -model overestimates emission within  $R_{500}$ , while underestimating emission at the center significantly (highlighted by a green arrow in Figure 4.6). The latter can be attributed to the absence of a second  $\beta$ -component, as a single  $\beta$ -model often inadequately describes the inner core emission, which is often higher-than-expected. (Sun et al., 2003) report, however, that even a two  $\beta$ -fit is not sufficient to describe the surface brightness within the central 1 kpc. Disregarding the excess emission within the core, no significant substructure or features can be noticed from the residual image.

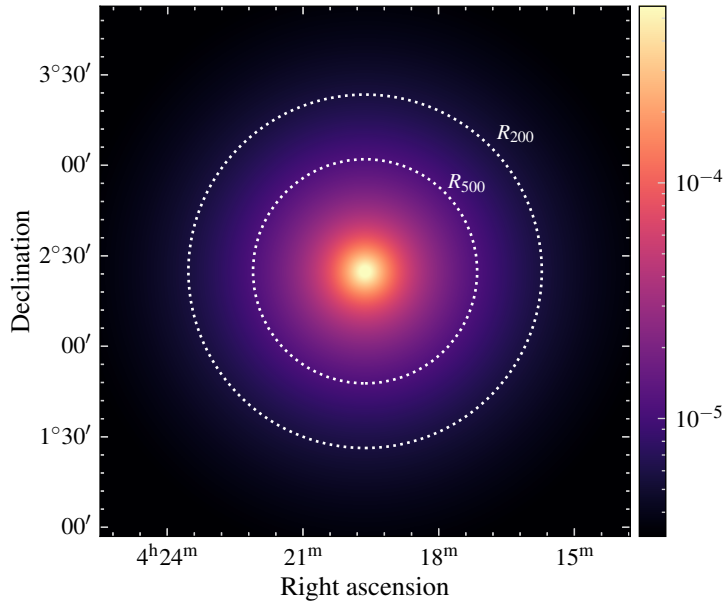


Figure 4.5:  $\beta$ -model image of NGC1550 utilizing the parameters in 4.2. The color bar represents counts per second.

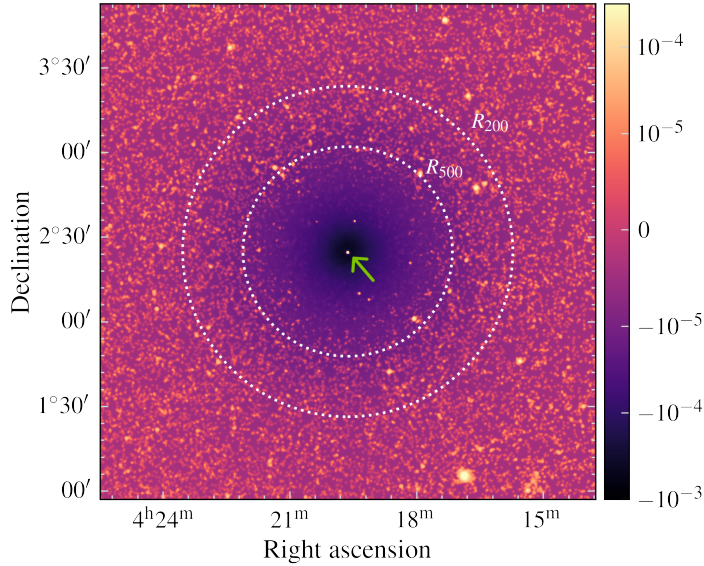


Figure 4.6: Residual image of NGC1550 derived by subtracting  $\beta$ -model image from the corrected soft-band image. The color bar represents counts per second and the image has been smoothed with a Gaussian-kernel of 5 pixels. The residual image indicate that the  $\beta$ -model slightly overestimates the emission around the core, due to the inadequacy of a single  $\beta$ -model in capturing the core's emission.

### 4.3 Sectoral Surface Brightness Analysis

Thus far, the surface brightness analysis has encompassed the entire azimuthal extent of the group. By analyzing surface brightness within specific sectors and comparing them to the full azimuthal profile, elongation in certain directions can be revealed. Various authors have reported an east-west elongation at the center of NGC1550 (Sun et al., 2003, Kolokythas et al., 2020), making it particularly interesting to determine whether this elongation extends into the outer regions of the group. To investigate this, four sectoral regions (north, south, east, and west) are divided into annuli, as shown in Figure 4.2. The center, width and extension of the annuli remain as described in Section 4.1, and surface brightness calculations and  $\beta$ -model fitting follow the same methodology.

Each region is initially fitted individually. Thereafter, the north and south sectors are combined for fitting, as are the east and west sectors. Figure 4.7(a) illustrates the comparison between the east and west profiles and Figure 4.7(b) compares the north and south profiles. The top graph in each figure shows the surface brightness profiles, including the observationally determined sky background and the corresponding  $\beta$ -model. The lower two graphs display the relative surface brightness differences of each region ( $SB_{sec}$ ) compared to the full azimuthal surface brightness profile ( $SB_{an}$ ). The error bars represent the error of the relative difference computed by Gaussian error propagation. The fit parameters for each  $\beta$ -model are listed in Table 4.3.

The fits are of lower quality when compared to the full azimuthal  $\beta$ -model fit ( $\chi^2/\text{d.o.f.} \lesssim 0.8$ ), suggesting possible overfitting or, more likely, an overestimation of the errors as attempts using wider  $2'$  annuli resulted in significantly improved  $\chi^2/\text{d.o.f.} \gtrsim 0.95$  for the west, north, and combined

east-west profiles, and a modest improvement for the remaining sectors. However, since the full azimuthal analysis was only performed with the smaller annuli and the resulting fit parameters were similar across both cases, the smaller annuli will be utilized for the following comparison.

When inspecting the western region, the emission dip observed in the western region between approximately  $390''$  and  $810''$  – as noted in section 4.1 – is noticeable in relation to the full azimuthal surface brightness profile. However, these deviations are not quantitatively significant and may be attributed to statistical fluctuations. For the northern and southern sectors, a significant deviation is noted at the first data point. This discrepancy is likely due to a suboptimal choice of the SB-center and is probably not physically significant, which shall be elaborated further below. In all sectors, however, no notable deviation from the full azimuthal profile is observed beyond  $390'$ . The combined east-west and north-south emissions are compared in Figure 4.8 with the  $\beta$ -model parameters being listed in Table 4.3. Here, too, no significant deviation from the full azimuthal profile is observed beyond the first data points, indicating that the east-west elongation observed within  $390''$  in Section 4.1 does not extend towards the outskirts of the group. The east-west elongation within  $390''$  can not be quantitatively confirmed, as only the third annulus shows an appreciable deviation compared to the combined north-south profile. This is complicated further by the potentially misplaced SB-center (*vide infra*) and the wide annuli, which set an arbitrary data resolution.

| Parameter   | $S_0 / \text{cts s}^{-1} \text{arcsec}^{-2}$ | $\beta$                          | $r_c / ''$                    | $d / \text{cts s}^{-1} \text{arcsec}^{-2}$ | $\chi^2/\text{d. o. f}$ |
|-------------|--|----------------------------------|-------------------------------|--|-------------------------|
| East-West   | $(2.88 \pm 0.27) \times 10^{-5}$             | $(5.08 \pm 0.12) \times 10^{-1}$ | $(8.60 \pm 0.80) \times 10^1$ | $(1.02 \pm 0.05) \times 10^{-7}$           | 0.83                    |
| North-South | $(6.20 \pm 0.71) \times 10^{-5}$             | $(4.58 \pm 0.07) \times 10^{-1}$ | $(4.01 \pm 0.43) \times 10^1$ | $(8.45 \pm 0.46) \times 10^{-8}$           | 0.71                    |
| West        | $(3.42 \pm 0.42) \times 10^{-5}$             | $(5.20 \pm 0.16) \times 10^{-1}$ | $(8.11 \pm 0.98) \times 10^1$ | $(9.63 \pm 0.60) \times 10^{-8}$           | 0.77                    |
| East        | $(3.18 \pm 0.43) \times 10^{-5}$             | $(4.87 \pm 0.15) \times 10^{-1}$ | $(7.22 \pm 0.97) \times 10^1$ | $(1.02 \pm 0.07) \times 10^{-7}$           | 0.82                    |
| North       | $(2.23 \pm 0.35) \times 10^{-5}$             | $(4.49 \pm 0.14) \times 10^{-1}$ | $(6.6 \pm 1.1) \times 10^1$   | $(7.89 \pm 0.78) \times 10^{-8}$           | 0.78                    |
| South       | $(1.10 \pm 0.20) \times 10^{-4}$             | $(4.69 \pm 0.10) \times 10^{-1}$ | $(3.32 \pm 0.53) \times 10^1$ | $(8.69 \pm 0.64) \times 10^{-8}$           | 0.86                    |

Table 4.3: Fit parameters, their errors, and the reduced chi-squared value for the  $\beta$ -model fit of the north, south, east and west sectors and the combined north-south and east-west sectors.

It is notable that the  $\beta$  parameter and the core radius  $r_c$  are not always consistent when comparing the sectors against each other and with the full azimuthal profile. For example, the core radius  $r_c$  for the combined east-west region is more than twice as large as that for the combined north-south region, and the  $\beta$  value is approximately 10% larger, with discrepancies at  $> 5\sigma$  and  $> 3\sigma$ , respectively. In fact, most of the  $\beta$ -values and core radii are inconsistent within  $1\sigma$  when comparing the sectors against each other. This discrepancy may indicate a poor SB-center choice, which is biasing the surface brightness towards the south. For instance, the southern sector's normalization factor  $S_0$  shows a relative difference of almost 80% compared to the north sector, with a  $4.32\sigma$  deviation. Consequently, the estimated SB-center at  $64.909^\circ$  and  $2.415^\circ$  is likely too far north, leading to an overestimation of southern emission in the initial data points, which is clearly visible in Figure 4.7(b). This problem is probably exacerbated by the wide  $1'$  annuli, meaning that excess emission from the first data point could significantly affect the fits. However, it is unclear why exactly the flux-weighted average method for SB center determination mentioned at the beginning of section 4.2 was unsatisfactory. Attempts using different aperture sizes and centering positions values and centering positions lead to very similar results.

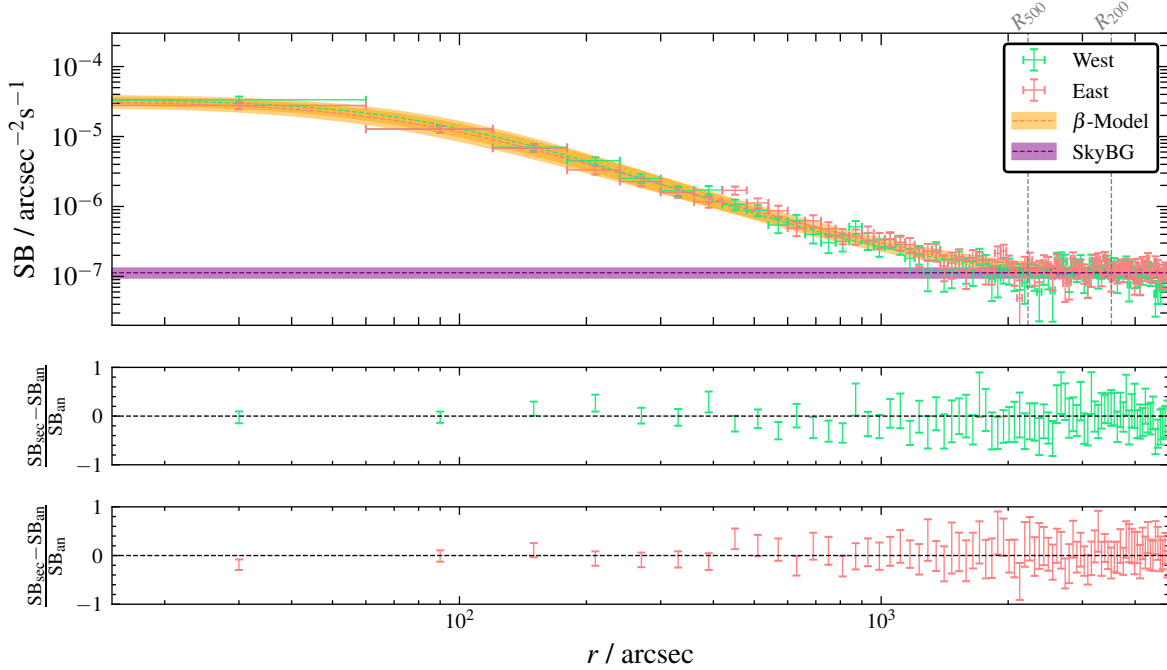
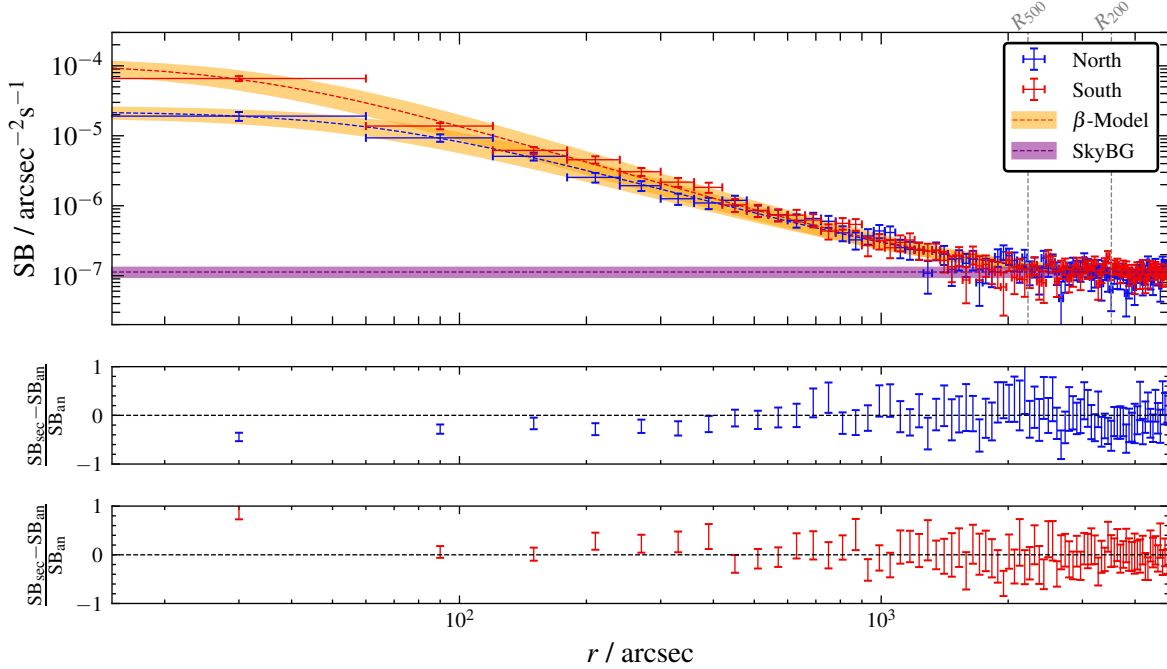

 (a)  $\beta$ -model fits for the West and East regions.

 (b)  $\beta$ -model fits for the North and South regions.

Figure 4.7:  $\beta$ -model fits for the West-East and North-South regions. *Top of each panel:* Surface brightness profiles, including the observationally determined sky background. *Bottom of each panel:* Relative surface brightness differences between each region ( $SB_{sec}$ ) and the full azimuthal surface brightness profile ( $SB_{an}$ ).

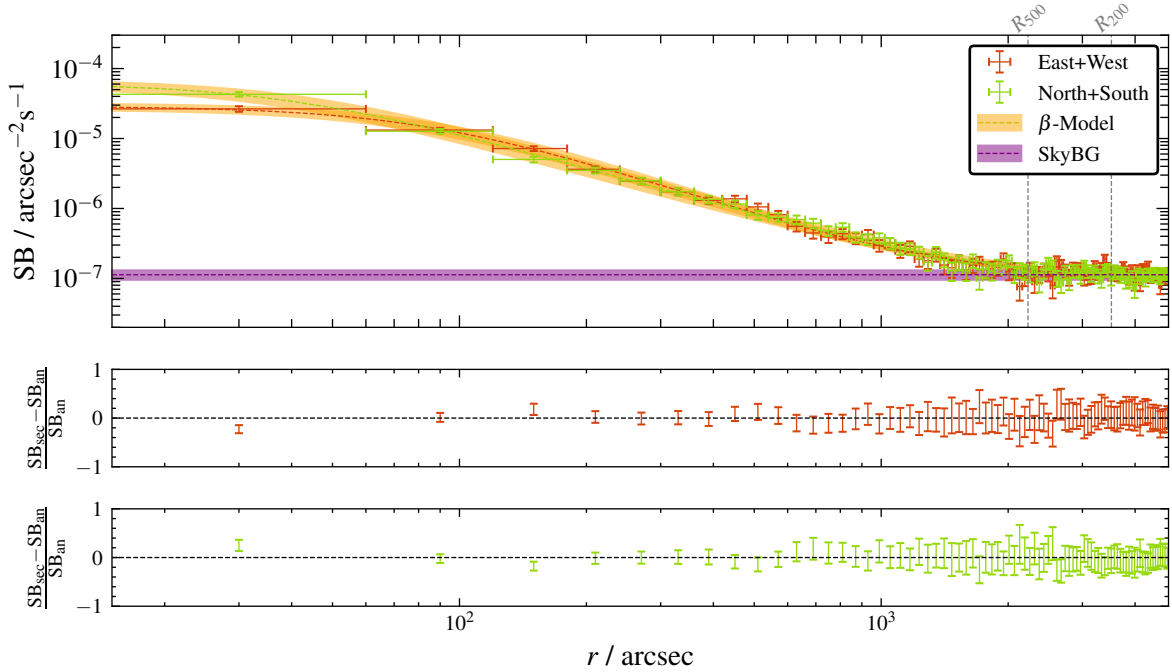


Figure 4.8:  $\beta$ -model fits for the combined east-west and north-south regions. The surface brightness profile is shown in the top graph and the lower two graphs display the relative surface brightness differences between each region ( $SB_{sec}$ ) and the full azimuthal surface brightness profile ( $SB_{an}$ ). Error bars are derived from Gaussian error propagation. Excluding the first data point, both combined surface brightness profiles show no significant deviation from the full azimuthal profile and are entirely consistent with each other, indicating no significant east-west elongation in the outskirts of the galaxy group.

Regarding the background, the fitted background level is in agreement with the total background level for the east, west and combined east-west regions. However, for the north and south regions, the fitted background level underestimates the observationally determined north and south backgrounds by 31% and 46%, at  $1.9\sigma$  and  $0.98\sigma$ , respectively. This discrepancy might be simply due to the inherently complex background of the Orion-Eridanus superbubble, though it can also be taken as an indication that the circles chosen for background estimation in Figure 4.3 are not far enough from the SB-center.

In general, such deviations in fit parameters would align well with the common notion that galaxy groups never exhibit perfect azimuthal symmetry, since infalling matter inevitably causes irregularities. Due to the aforementioned issue regarding the SB-center, one can not conclusively take the fit deviations of the sectoral surface brightness analysis as confirmation for this view. Regardless, the sectoral surface profiles confirm that no significant deviations from azimuthal symmetry can be established in the outskirts, were the above mentioned issues of the SB-center and annuli width are largely insignificant, and contamination from the background dominates.

# CHAPTER 5

---

## Conclusion

---

The aim of this thesis was the characterization of the X-ray morphology of the galaxy group NGC1550 through detailed surface brightness analysis. After correcting and reducing the raw photon data obtained from eRASS:1 in Chapter 3, Chapter 4 began with qualitative inspection of the corrected data. A contour plot of the corrected, cheese-masked wavelet filtered image in the soft-band with an overlaid galaxy distribution was shown (Figure 4.1). From this figure, it was visually established that the galaxy group NGC1550 appears relaxed and spherically symmetrical. Furthermore, using a contour plot of the corrected soft-band image (Figure 4.2), some indications of asymmetry were visually identified within  $810''$ . Emission was found to drop off to background levels at  $R_{500}$  and a complex background was noted, which can be attributed to the Orion-Eridanus superbubble. No obvious correlation between the X-ray contours and the galaxy distribution could be ascertained.

To more accurately characterize the morphology of NGC1550 in the X-ray, surface brightness analysis was performed. A beta model was fitted to characterize the full azimuthal profile, as shown in Figure 4.4. The model fitting yielded a  $\beta$ -value of  $0.478 \pm 0.008$  and a core radius of  $r_c = (60 \pm 5)'' \approx (15 \pm 2) \text{ kpc}$  with a reduced chi-squared value of 0.96, indicating a good fit. This result was consistent with the findings of previous studies, showing that the eROSITA view of NGC1550 aligns with previous findings. The full azimuthal surface brightness profile showed no significant deviations from spherical symmetry. Moreover, the sectoral surface brightness analysis across the north, south, east, and west sectors, as well as the combined north-south and east-west sectors, also revealed no significant deviations from azimuthal symmetry beyond  $390''$ .

The residual image indicated that the beta model does not described emission within  $R_{500}$  accurately, underestimating the core emission, as is common, and no features were detected. Attempts to use a two beta model were unsuccessful, likely due to the large width of the annuli and the small inner core component, which, from previous studies (Kawaharada, Makishima, Kitaguchi, et al., 2009), is of order of eROSITA's angular resolution.

Within  $390''$ , the qualitatively observed east-west elongation could not be quantitatively confirmed by the surface brightness analysis. Although the sectoral surface brightness profiles did not differ significantly from the azimuthal profile, their fit parameters often varied significantly and the individual beta fits of each sector were of slightly lower quality ( $\chi^2 \lesssim 0.8$ ). It was speculated that these issues were caused by the fairly wide  $1'$  annulli and due to a poor choice of the SB-center, resulting in a

significant discrepancy between the north and south emission for the first data point at  $\sim 1'$ . The surface brightness analysis also highlighted a slight discrepancy between the observationally estimated backgrounds and the fitted background levels, suggesting that background estimation could have been performed with greater care.

## 5.1 Outlook

After analyzing the results of this thesis, some suggestions for improvement can be made. The SB-center could have been determined more precisely, either manually or, better, by a two-dimensional beta fit of the full azimuthal profile, allowing it to be freely fitted. A comparison using the brightest pixel as the SB-center is ongoing work and will be presented at a later date. Better background estimation using different background regions could also have been attempted, and visualization of the background gradient by plotting the background emission of each circular region may also be interesting.

Furthermore, because only eRASS:1 data was utilized, several features observed qualitatively, such as a slight emission dip in the western sector between  $\sim 390''$  and  $\sim 810''$ , could not be verified quantitatively. With additional data, such as from eRASS:4, these features could be more accurately interpreted and their significance better assessed. The increased data would also allow for finer annuli in the surface brightness analysis due to the higher count rates in each annulus bin, thus facilitating feature identifications. Although no evidence was found in this work, additional data with better statistics may reveal other features in the soft-band, such as filaments in the outskirts (Cen and Ostriker, 1999). Additionally, enabled by eROSITA's wide field of view and great sensitivity in the soft-band, future work could study superbubbles such as Orion-Eridanus, as has been done in previous studies with ROSAT data (Krause et al., 2014).

# **Appendix**

# APPENDIX A

---

## Data Reduction

---

### A.1 Exposure maps

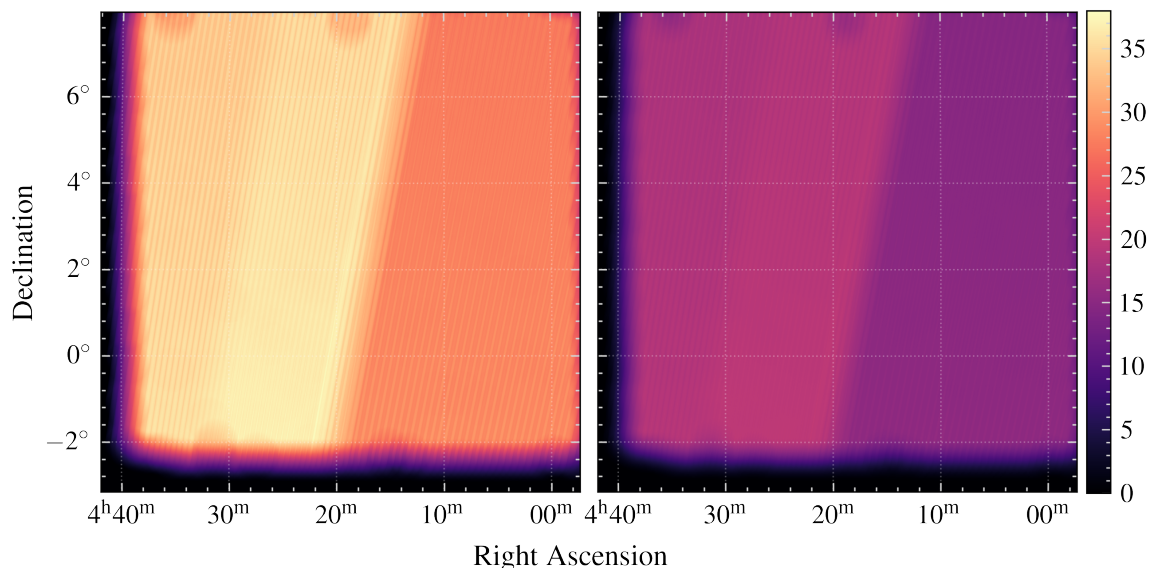


Figure A.1: Soft-bad exposure map for TM1 created in Section 3.3. *Left:* flat exposure map. *Right:* vignetted exposure map. The color bar units are seconds.

## Appendix A Data Reduction

---

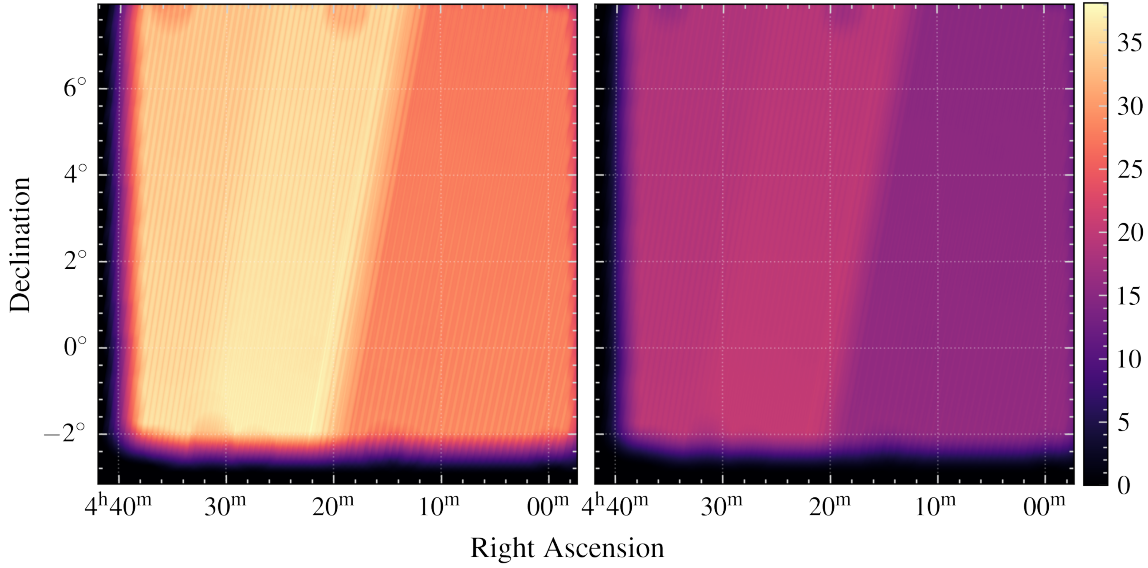


Figure A.2: Soft-bad exposure map for TM2 created in Section 3.3. *Left:* flat exposure map. *Right:* vignetted exposure map. The color bar units are seconds.

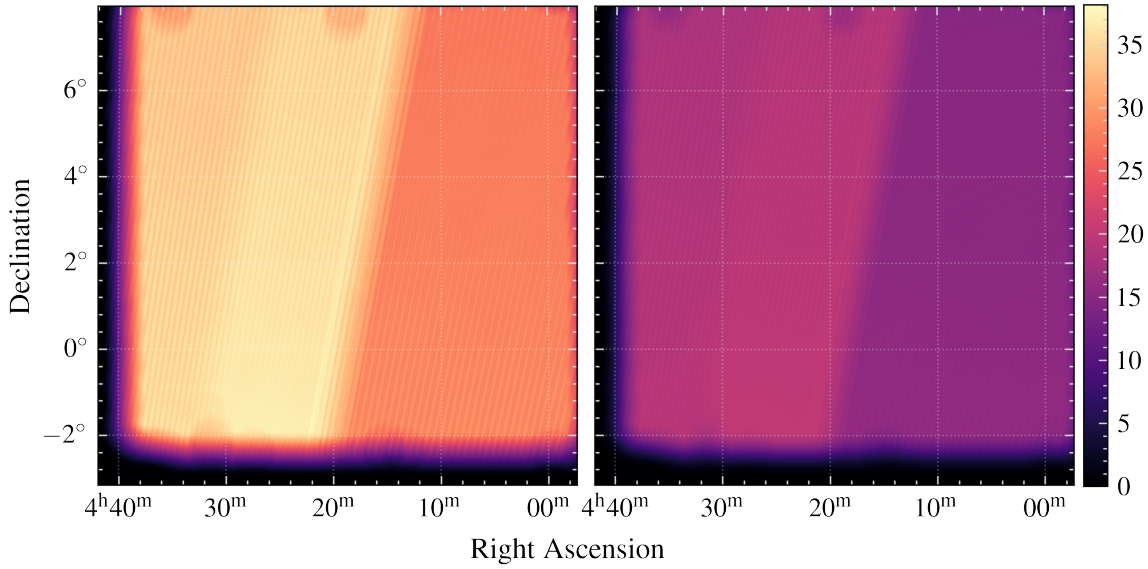


Figure A.3: Soft-bad exposure map for TM3 created in Section 3.3. *Left:* flat exposure map. *Right:* vignetted exposure map. The color bar units are seconds.

---

## Appendix A Data Reduction

---

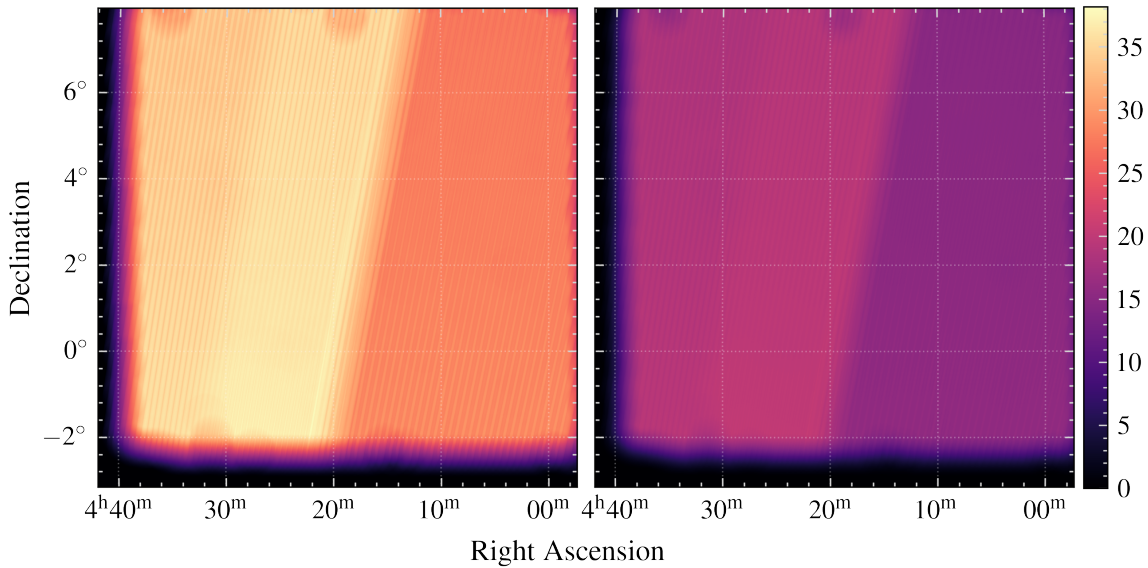


Figure A.4: Soft-bad exposure map for TM4 created in Section 3.3. *Left:* flat exposure map. *Right:* vignetted exposure map. The color bar units are seconds.

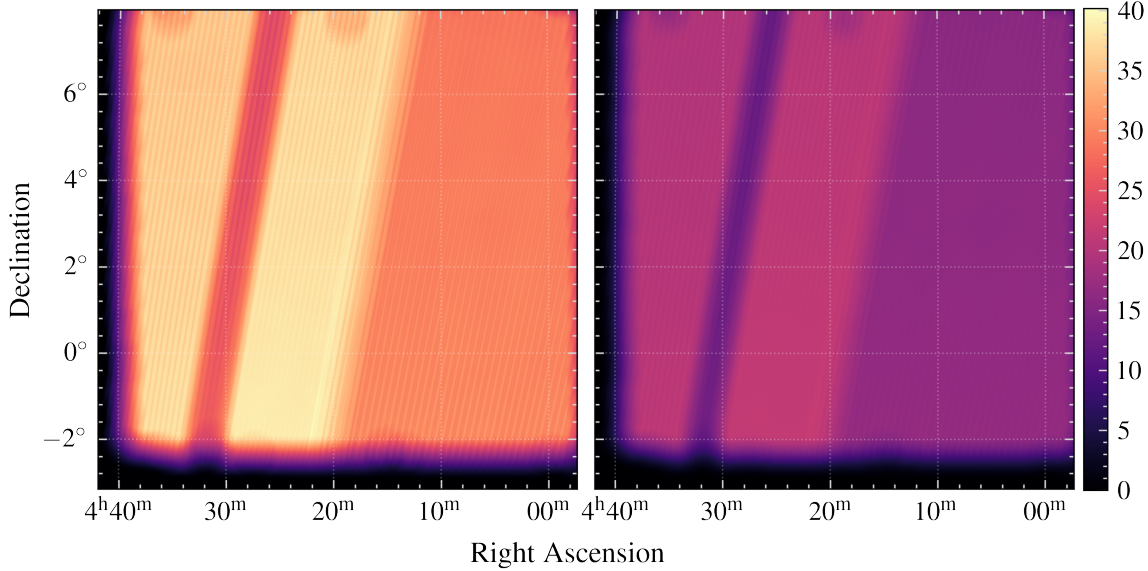


Figure A.5: Soft-bad exposure map for TM5 created in Section 3.3. *Left:* flat exposure map. *Right:* vignetted exposure map. The color bar units are seconds.

---

## Appendix A Data Reduction

---

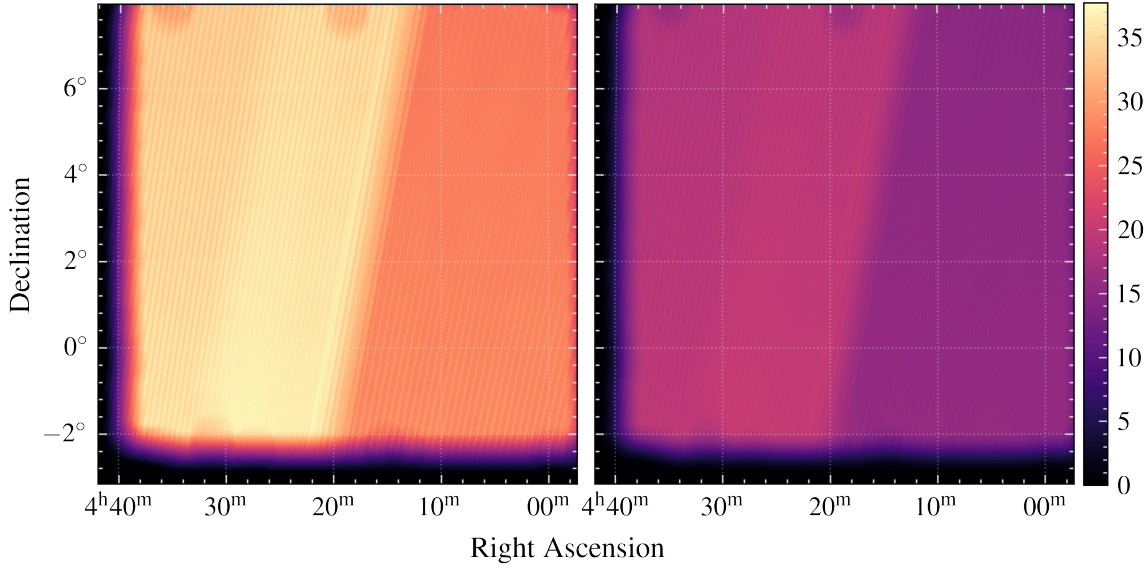


Figure A.6: Soft-bad exposure map for TM6 created in Section 3.3. *Left:* flat exposure map. *Right:* vignetted exposure map. The color bar units are seconds.

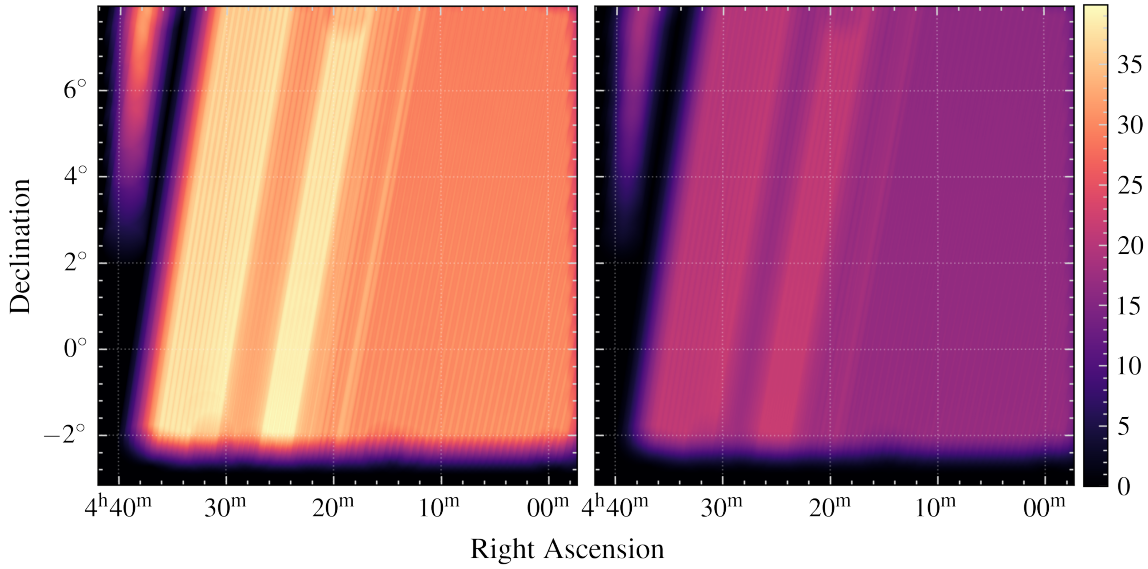


Figure A.7: Soft-bad exposure map for TM7 created in Section 3.3. *Left:* flat exposure map. *Right:* vignetted exposure map. The color bar units are seconds.

---

## Appendix A Data Reduction

---

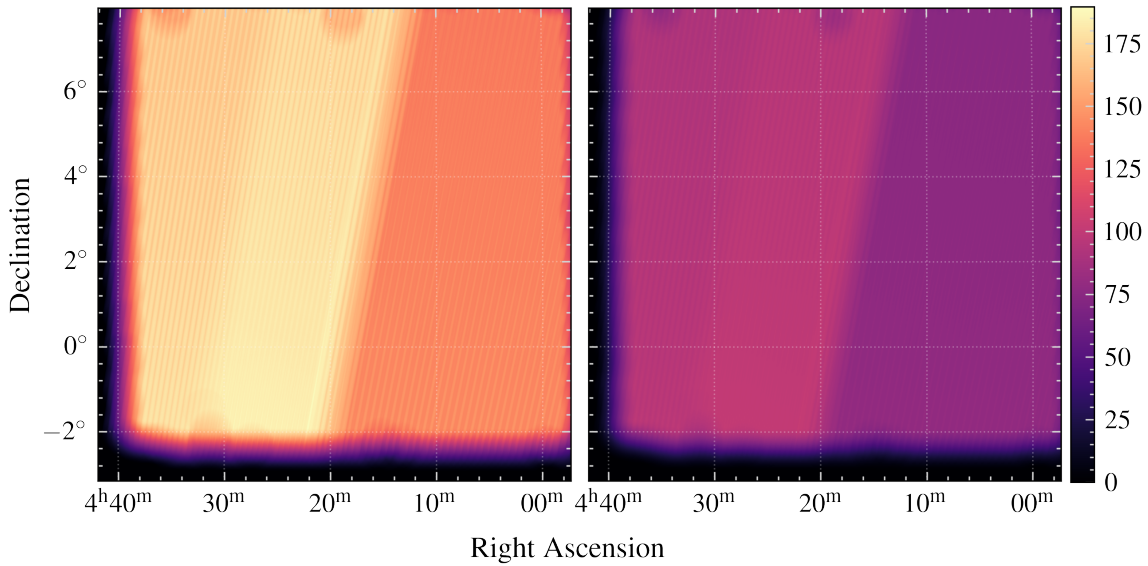


Figure A.8: Soft-bad exposure map for TM8 created in Section 3.3. *Left:* flat exposure map. *Right:* vignetted exposure map. The color bar units are seconds.

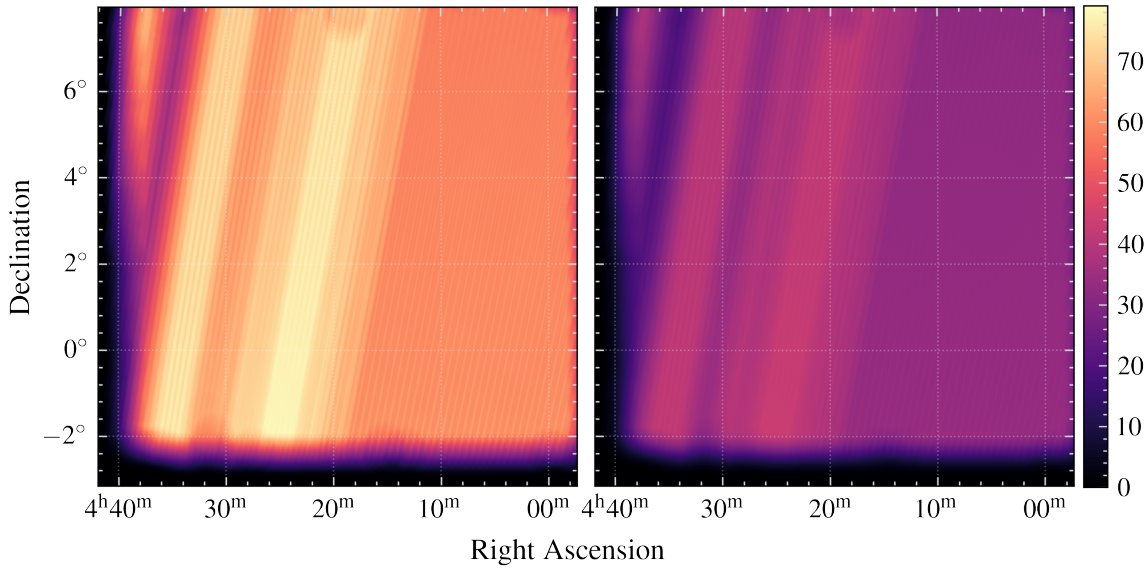


Figure A.9: Soft-bad exposure map for TM9 created in Section 3.3. *Left:* flat exposure map. *Right:* vignetted exposure map. The color bar units are seconds.

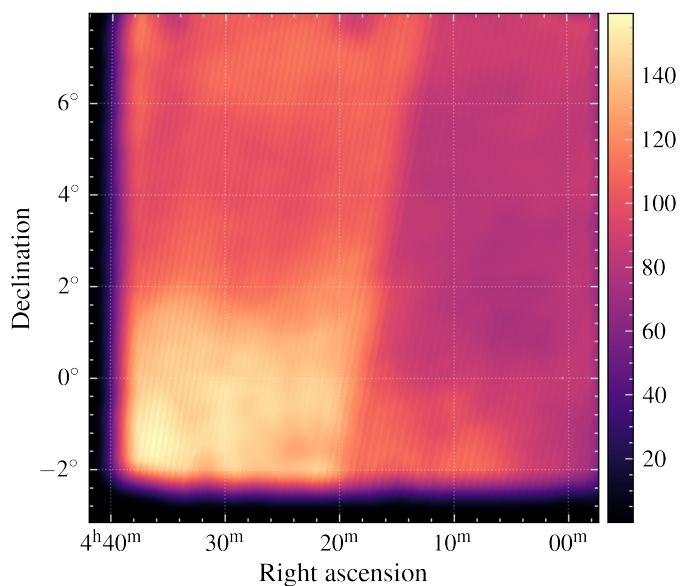


Figure A.10: Fully corrected, soft-bad exposure map for TM0 obtained by the procedures outlined in Section 3.6. *Left:* flat exposure map. *Right:* vignetted exposure map. The color bar units are seconds.

## A.2 PIB Map

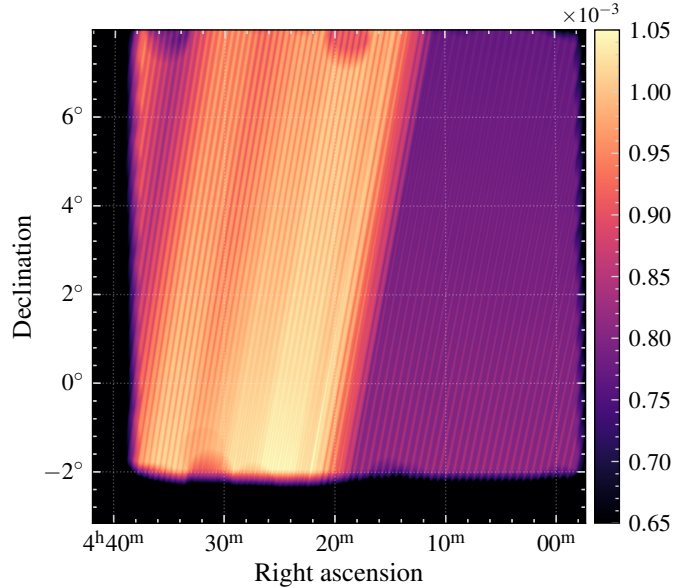


Figure A.11: PIB-map created by co-adding individual background maps for each telescope module (TM) as outlined in Section 3.4.

| TM | R    | $H_{\text{obs}}$ |
|----|------|------------------|
| 1  | 1.30 | 9512             |
| 2  | 1.36 | 8362             |
| 3  | 1.35 | 9187             |
| 4  | 1.24 | 10177            |
| 5  | 0.85 | 10817            |
| 6  | 1.29 | 9144             |
| 7  | 0.82 | 10214            |

Table A.1: Values of  $R$ , and  $H_{\text{obs}}$  utilized for the PIB-correction in Section 3.4

### A.3 Orion-Eridanus Superbubble

To better link the background gradient observed in the wavelet-filtered image (Figure 4.3) to the Orion-Eridanus superbubble, the ROSAT X-ray map of the Orion-Eridanus region presented by Krause et al. (2014) and described in Section 2.3 was replaced by a cutout of the wavelet-filtered image at the position of NGC1550. For this, the orientation of the latter was changed to match the galactic coordinates present in the former. The result can be seen in Figure A.12. It is evident that the background gradient present in the eROSITA data lines up well with the gradient direction of the Orion-Eridanus superbubble.

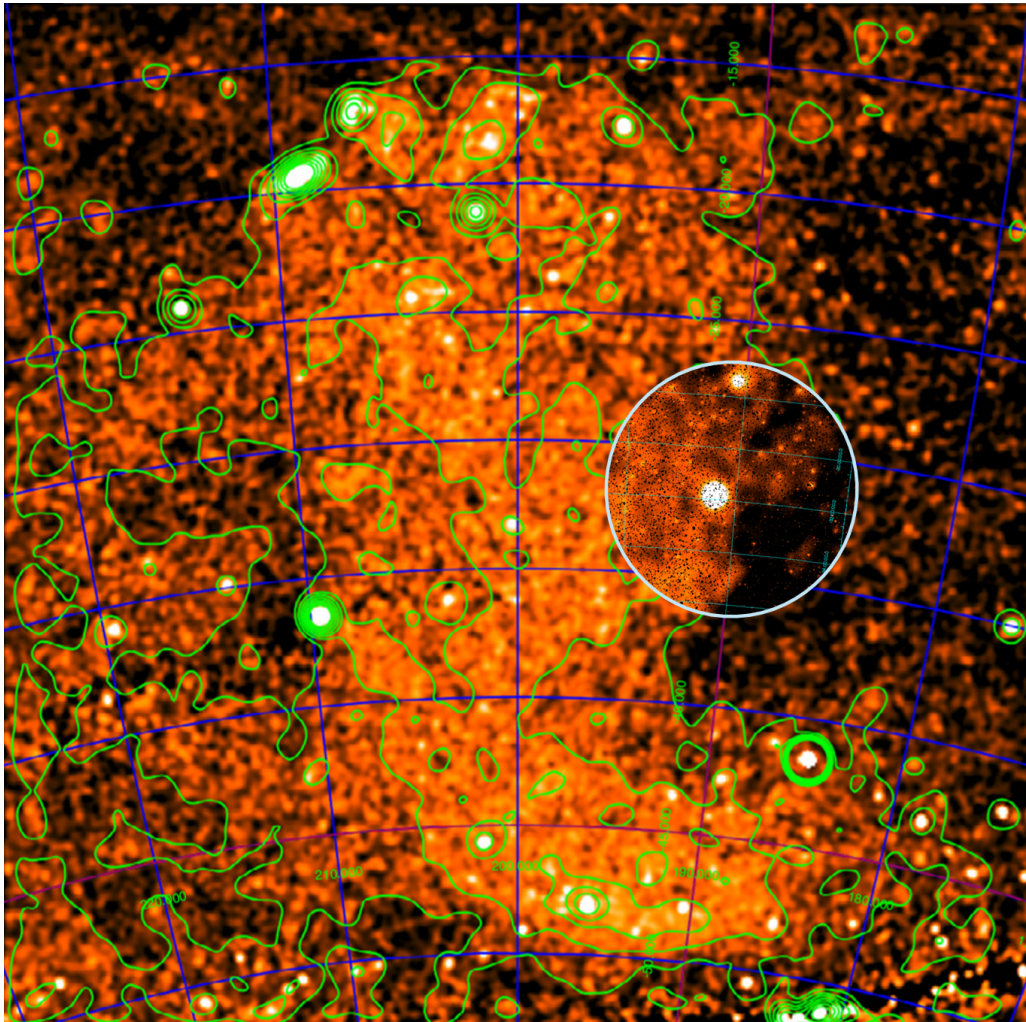


Figure A.12: Wavelet-filtered, soft-band image obtained in this thesis (white circle) cutout and reprojected onto the ROSAT X-ray map of the Orion-Eridanus superbubble taken from Krause et al. (2014). For visualization purposes, the color schemes were matched.

---

## Bibliography

---

- Arnaud, K. A. (1996), *XSPEC: The First Ten Years*, Astronomical Society of the Pacific Conference Series **101** 17, ed. by G. H. Jacoby and J. Barnes (cit. on p. 9).
- Bertin, E. and S. Arnouts (1996), *SExtractor: Software for source extraction.*, *Astronomy and Astrophysics Supplement* **117** 393 (cit. on p. 11).
- Böhringer, H. et al. (2000), *The Northern ROSAT All-Sky (NORAS) Galaxy Cluster Survey. I. X-Ray Properties of Clusters Detected as Extended X-Ray Sources*, *The Astrophysical Journal Supplement Series* **129** 435, arXiv: [astro-ph/0003219 \[astro-ph\]](#) (cit. on pp. 1, 3).
- Brandt, W. N. and G. Hasinger (2005), *Deep Extragalactic X-Ray Surveys*, *Annual Review of Astronomy & Astrophysics* **43** 827, arXiv: [astro-ph/0501058 \[astro-ph\]](#) (cit. on p. 4).
- Bulbul, E. et al. (2020), *Characterization of the Particle-induced Background of XMM-Newton EPIC-pn: Short- and Long-term Variability*, *The Astrophysical Journal* **891** 13, URL: <https://dx.doi.org/10.3847/1538-4357/ab698a> (cit. on p. 5).
- Cavaliere, A. and R. Fusco-Femiano (1976), *X-rays from hot plasma in clusters of galaxies.*, *Astronomy and Astrophysics* **49** 137 (cit. on p. 3).
- Cavaliere, A. G., H. Gurksy, and W. H. Tucker (1971), *Extragalactic X-ray Sources and Associations of Galaxies*, *Nature* **231** 437, ISSN: 1476-4687, URL: <https://doi.org/10.1038/231437a0> (cit. on p. 2).
- Cen, R. and J. P. Ostriker (1999), *Where Are the Baryons?* *The Astrophysical Journal* **514** 1, URL: <https://dx.doi.org/10.1086/306949> (cit. on p. 24).
- Davis, J. E. (2001), *The Formal Underpinnings of the Response Functions Used in X-Ray Spectral Analysis*, *The Astrophysical Journal* **548** 1010, URL: <https://dx.doi.org/10.1086/319002> (cit. on p. 9).
- Fukugita, M., C. J. Hogan, and P. J. E. Peebles (1998), *The Cosmic Baryon Budget*, *The Astrophysical Journal* **503** 518, arXiv: [astro-ph/9712020 \[astro-ph\]](#) (cit. on p. 1).
- Galeazzi, M., A. Gupta, K. Covey, and E. Ursino (2007), *XMM-Newton Observations of the Diffuse X-Ray Background*, *The Astrophysical Journal* **658** 1081, URL: <https://dx.doi.org/10.1086/512032> (cit. on p. 4).
- HI4PI Collaboration et al. (2016), *HI4PI: A full-sky HI survey based on EBHIS and GASS*, *Astronomy & Astrophysics* **594** A116, URL: <https://ui.adsabs.harvard.edu/abs/2016A&A...594A.116H> (cit. on p. 8).
- Jones, L. et al. (2003), *The nature and space density of fossil groups of galaxies*, *Monthly Notices of the Royal Astronomical Society* **343** (cit. on p. 3).

## Bibliography

---

- Kawaharada, M., K. Makishima, T. Kitaguchi, et al. (2009), *A GALAXY MERGER SCENARIO FOR THE NGC 1550 GALAXY FROM METAL DISTRIBUTIONS IN THE X-RAY EMITTING PLASMA*, *The Astrophysical Journal* **691** 971, URL: <https://dx.doi.org/10.1088/0004-637X/691/2/971> (cit. on pp. 1, 3, 17, 23).
- Kawaharada, M., K. Makishima, I. Takahashi, et al. (2003), *A New Candidate for the Dark Group of Galaxies, RX J0419+0225*, *Publications of the Astronomical Society of Japan* **55** 573 (cit. on pp. 1, 3, 17).
- King, I. (1962), *The structure of star clusters. I. an empirical density law*, *Astronomical Journal* **67** 471 (cit. on p. 3).
- Kolokythas, K. et al. (2020), *Evidence of AGN feedback and sloshing in the X-ray luminous NGC 1550 galaxy group*, *Monthly Notices of the Royal Astronomical Society* **496** 1471, ISSN: 0035-8711, URL: <https://doi.org/10.1093/mnras/staa1506> (cit. on pp. 4, 19).
- Krause, M., R. Diehl, H. Böhringer, M. Freyberg, and D. Lubos (2014), *Feedback by massive stars and the emergence of superbubbles: II. X-ray properties*, *Astronomy & Astrophysics* **566** A94, ISSN: 1432-0746, URL: <http://dx.doi.org/10.1051/0004-6361/201423871> (cit. on pp. 4, 5, 24, 33).
- Kravtsov, A. V. and S. Borgani (2012), *Formation of Galaxy Clusters*, *Annual Review of Astronomy and Astrophysics* **50** 353, ISSN: 0066-4146, URL: <https://www.annualreviews.org/doi/10.1146/annurev-astro-081811-125502> (cit. on pp. 1, 2).
- Pacaud, F. et al. (2006), *The XMM Large-Scale Structure survey: the X-ray pipeline and survey selection function*, *Monthly Notices of the Royal Astronomical Society* **372** 578, ISSN: 0035-8711, eprint: <https://academic.oup.com/mnras/article-pdf/372/2/578/2937517/mnras0372-0578.pdf>, URL: <https://doi.org/10.1111/j.1365-2966.2006.10881.x> (cit. on p. 10).
- Predehl, P. et al. (2021), *The eROSITA X-ray telescope on SRG*, *A&A* **647** A1, URL: <https://doi.org/10.1051/0004-6361/202039313> (cit. on pp. 4, 5, 17).
- Reiprich, T. H., A. Veronica, et al. (2021), *The Abell 3391/95 galaxy cluster system: A 15 Mpc intergalactic medium emission filament, a warm gas bridge, infalling matter clumps, and (re-) accelerated plasma discovered by combining SRG/eROSITA data with ASKAP/EMU and DECam data*, *Astronomy & Astrophysics* **647** A2, URL: <https://doi.org/10.1051/0004-6361/202039590> (cit. on pp. 8, 10).
- Reiprich, T. H. and H. Böhringer (2002), *The Mass Function of an X-Ray Flux-limited Sample of Galaxy Clusters*, *The Astrophysical Journal* **567** 716, URL: <https://dx.doi.org/10.1086/338753> (cit. on pp. 3, 6, 17).
- Reiprich, T. H. and F. Pacaud (2019), *Multiwavelength Observations of Galaxy Clusters*, (cit. on p. 3).
- Sato, K. et al. (2010), *Metallicity of the Fossil Group NGC 1550 Observed with Suzaku*, *Publications of the Astronomical Society of Japan* **62** 1445, arXiv: [1009.4173 \[astro-ph.CO\]](https://arxiv.org/abs/1009.4173) (cit. on pp. 1, 4).
- Schneider, P. (2006), *Extragalactic Astronomy and Cosmology: An Introduction*, Second Edition, Springer-Verlag Berlin Heidelberg 2006, ISBN: 978-3-642-54082-0 (cit. on pp. 1, 2).
- Starck, J.-L. and Pierre, M. (1998), *Structure detection in low intensity X-ray images*, *Astronomy and Astrophysics Supplement* **128** 397, URL: <https://doi.org/10.1051/aas:1998150> (cit. on p. 11).

## Bibliography

---

- Sun, M. et al. (2003), *Chandra Observations of the NGC 1550 Galaxy Group: Implication for the Temperature and Entropy Profiles of 1 keV Galaxy Groups*, *The Astrophysical Journal* **598** 250, URL: <https://dx.doi.org/10.1086/378887> (cit. on pp. 1, 3, 4, 17–19).
- Veronica, A. (2020), *X-ray Studies of the Interacting Galaxy Cluster System Abell 3391 and Abell 3395 Using eROSITA and XMM-Newton*, Masterthesis in Astrophysics, MA thesis: Argelander-Institut für Astronomie, Mathematisch-Naturwissenschaftliche Fakultät der the Rheinischen Friedrich-Wilhelms-Universität Bonn (cit. on p. 8).
- Willingale, R., R. L. C. Starling, A. P. Beardmore, N. R. Tanvir, and P. T. O'Brien (2013), *Calibration of X-ray absorption in our Galaxy*, *Monthly Notices of the Royal Astronomical Society* **431** 394, arXiv: [1303.0843 \[astro-ph.HE\]](https://arxiv.org/abs/1303.0843) (cit. on pp. 5, 8).

---

# List of Figures

---

|      |  |    |
|------|--|----|
| 2.1  | X-ray map in galactic coordinates of the Orion-Eridanus superbubble.   | 5  |
| 3.1  | Raw photon images from TM0 of all combined skytiles centered around NGC1550 displayed at different energy bands. | 7  |
| 3.2  | $N_{\text{Htot}}$ -map.  | 9  |
| 3.3  | Comparison between the filtered, full energy-band count rate image and the final corrected, soft-band image.     | 11 |
| 3.4  | Corrected wavelet filtered image before and after applying the cheesemask.                                       | 12 |
| 3.5  | Workflow diagram of the data reduction procedures.   | 12 |
| 4.1  | Contour plot of the corrected, cheese-masked, wavelet-filtered image with overlaid galaxy distribution.          | 14 |
| 4.2  | Contour plot of the corrected soft-band image smoothed.  | 15 |
| 4.3  | Circular regions for background estimation.  | 16 |
| 4.4  | Full azimuthal surface brightness profile  | 17 |
| 4.5  | $\beta$ -model image of NGC1550.   | 18 |
| 4.6  | Residual image of NGC1550.   | 19 |
| 4.7  | $\beta$ -model fits for the West-East and North-South regions.   | 21 |
| 4.8  | $\beta$ -model fits for the combined east-west and north-south regions   | 22 |
| A.1  | Exposure maps for TM1.   | 26 |
| A.2  | Exposure maps for TM2.   | 27 |
| A.3  | Exposure maps for TM3.   | 27 |
| A.4  | Exposure maps for TM4.   | 28 |
| A.5  | Exposure maps for TM5.   | 28 |
| A.6  | Exposure maps for TM6.   | 29 |
| A.7  | Exposure maps for TM7.   | 29 |
| A.8  | Exposure maps for TM8.   | 30 |
| A.9  | Exposure maps for TM9.   | 30 |
| A.10 | Exposure maps for TM0.   | 31 |
| A.11 | PIB-map.   | 32 |
| A.12 | Reprojection of Wavelet-filtered image onto ROSAT X-ray map.   | 33 |

---

## List of Tables

---

|     |  |    |
|-----|--|----|
| 4.1 | Surface brightness and associated errors for the different background regions. . . . .   | 15 |
| 4.2 | Fit parameters for the full azimuthal surface brightness profile. . . . .  | 16 |
| 4.3 | Fit parameters for the $\beta$ -model fit of the north, south, east and west sectors and the combined north-south and east-west sectors. . . . . | 20 |
| A.1 | Values of $R$ , and $H_{\text{obs}}$ utilized for the PIB-correction in Section 3.4 . . . . .  | 32 |